

SINTEF Energi AS
SINTEF Energy Research
Address:

Sem Sælands vei 11
7034 Trondheim
NORWAY

Telephone: +47 73597200

energy.research@sintef.no
www.sintef.no/energi
Enterprise /VAT No:
NO 939 350 675 MVA

Project memo

Environmental Loads for Frequency-Domain Aeroelastic Analysis of Offshore Wind Turbines

VERSION

1.0

DATE

2015-04-13

AUTHOR(S)

Karl O. Merz

CLIENT(S)

NOWITECH

CLIENTS REF.

Addendum to DC.2-2

PROJECT NO.

502000059

NO. OF PAGES AND APPENDICES:

38 + appendices

ABSTRACT

Methods have been developed for the calculation of environmental loads, as input to the STAS wind power plant analysis program. A spectral model of rotationally-sampled atmospheric turbulence was extended using the multi-blade coordinate transformation. This gives the correct frequency spectra, dominated by multiples of $3P$, seen by the support structures. For wave loads on the foundation, the Morison equation was extended using a full first-order potential solution, which is valid when the pile diameter is on the same order as the wavelength. The computation of loads is performed in the time domain, and subsequently transformed to the frequency domain. The first-order velocity profiles are stretched to the instantaneous free-surface, and velocity-squared terms are retained in Bernoulli's equation, in order to capture the most important sum-frequency effects which may excite tower resonance. The method was validated by comparison against published calculations, laboratory experiments, and field measurements.

PREPARED BY

Karl O. Merz

APPROVED BY

Harald G. Svendsen

PROJECT MEMO NO.

AN 15.12.19

SIGNATURE



SIGNATURE



CLASSIFICATION

Unrestricted

Document history

VERSION	DATE	VERSION DESCRIPTION
1.0	2015-04-13	Original document

Table of contents

1	Frequency-Domain Analysis of Wind Turbines	4
2	Atmospheric Turbulence	4
2.1	Single-Point Spectrum	5
2.2	Correlations in Space and Time	7
2.3	Correlations in Multi-Blade Coordinates	11
3	Wave Loads	14
3.1	Wave Climate	15
3.1.1	Joint Probabilities of H_s and T_p	16
3.1.2	Wave Amplitude Spectra	16
3.2	Wave Kinematics and First-Order Potential	16
3.2.1	Incident Wave Potential	17
3.2.2	Total Linear Potential	20
3.3	Pressure Forces	25
3.3.1	Bernoulli's Equation	27
3.3.2	Surface-Elevation Effects	28
3.4	Load Spectra	29
3.5	Validation	30
3.6	Illustrative Results	34
4	Conclusions	36
	References	36

1 Frequency-Domain Analysis of Wind Turbines

STAS (State Space Analysis of Offshore Wind Power Plants) is a program for the dynamic analysis of wind power plants. The equations describing the wind power plant are linearized and incorporated into a unified, linear state space.

A complete model of an offshore wind power plant requires a description of the wind turbines, the electrical interconnections and transmission to shore, the environmental conditions, and the control systems. Merz [29] describes the model of the wind turbine aerodynamics and structures employed in the STAS program. The model is based on the theory of Hansen ([17],[18]), and is also similar to the TURBU Offshore program, as described by van Engelen *et al.* ([38],[39]).

One of the intended uses of STAS is the rapid, preliminary analysis of fatigue loads in the frequency domain. STAS is also intended to be used in the design and analysis of advanced control systems, which may receive data from sensors such as anemometers, strain gauges, and accelerometers. Such applications require an accurate representation of the environmental loads – turbulent winds and ocean waves and currents – and the response of the structures and electric systems.

The environmental load models employed in STAS are improved in comparison with those of existing frequency-domain codes. Atmospheric turbulence is modelled as isotropic, which is restrictive; but within this assumption, the full set of cross-correlations of rotationally-sampled axial and in-plane turbulence components is computed. Previous frequency-domain models have neglected the in-plane components. Taking the multi-blade coordinate transform gives the effective turbulence correlation functions, including the rotational sampling effect, as seen by the support structures. The correlation functions and associated spectra are dominated by multiples of the blade passing frequency.

Ocean wave and current load spectra are computed by a Morison-type method where the inertia and viscous drag loads are superposed. However, instead of using an inertia coefficient, the full first-order potential is computed, and loads are obtained by numerically integrating the pressure field. This approach gives accurate results both when the pile diameter is small – reproducing the Morison equation in this case – and when the pile diameter is on the same order as the wavelength, which is often the case for the components of (first-order) waves which are in the vicinity of the tower resonant frequencies. Second-order sum-frequency effects may also contribute to tower resonance. To partly capture these sum-frequency effects, the wave and current loads are computed in the time domain, including the velocity-squared terms in Bernoulli's equation for the fluid pressure; furthermore, the fluid velocity profiles are stretched to the instantaneous free surface. Nodal force spectra are computed from the time series, for use as input to frequency-domain analyses.

2 Atmospheric Turbulence

In time-domain aeroelastic analyses of wind turbine loads, it is typical to specify the turbulent velocity fluctuations at a set of points filling a space, which is then convected at a specified rate across the rotorplane. The windspeed at a given point and time is interpolated from the points on the grid.

As an alternative, correlation functions (time domain) and cross-spectra (frequency domain) can be computed for specified points on the rotating blades. Kristensen and Frandsen ([22],[23]), also Connell [9], describe models of this type.

Sørensen ([35],[36]) implements such a frequency-domain method to compute the aerodynamic loads on wind turbine rotors. An exponential decay function is used for the correlation of turbulence over distance. A key assumption of Sørensen's method is that the rotor is rotating quickly with respect to the characteristic frequency band of the turbulence, such that the

coherence upon completion of one full revolution is unity. This assumption is questionable in the case of a large wind turbine rotor, with a period of revolution on the order of 10 seconds.

Merz [28] extends the method of Kristensen and Frandsen to include the in-plane (tangential) component orthogonal to the blade span. This method is here extended to the case of multiple blades, and the multi-blade coordinate transform.

The input to the aerodynamic model is the turbulent velocity fluctuations seen by each blade element as it rotates. It is assumed that the turbulence is isotropic. This simplifies the mathematics, allowing the use of simple expressions to relate the stochastic properties at different points in space and at different times. Real turbulence is not isotropic: the lateral and vertical fluctuations tend to be of a lower magnitude than the axial (mean flow-direction) fluctuations. Defining the axial turbulence intensity as

$$I = \frac{\sigma_u}{V_\infty}, \quad (2.1)$$

typical values for the lateral and vertical turbulence intensity are $0.8I$ and $0.5I$, respectively [4]. The assumption of isotropic turbulence will therefore tend to overpredict the severity of the in-plane components. Comparisons of computed and measured spectra of loads at the root of a wind turbine blade indicate that the assumption of isotropic turbulence is not a severe limitation [27].

2.1 Single-Point Spectrum

The starting point is the von Karman spectrum for the axial turbulence at a single point in space [4],

$$S_{zz}^o(0, f) = \sigma_u^2 \frac{4L_u}{V_\infty \left[1 + 70.8(fL_u/V_\infty)^2 \right]^{5/6}} \quad (2.2)$$

where f is the frequency in Hz and

$$L_u = (280 \text{ m}) \left[\frac{H}{(1000h_0^{0.18}) \text{ m}} \right]^{0.35}. \quad (2.3)$$

Here H is the hub height and h_0 a "surface roughness length" to be calibrated based on the terrain conditions. In undisturbed offshore conditions, a typical value for h_0 is 0.0001 m. However, Meneveau [26] and Calaf *et al.* [5] provide evidence that the effective value may be much higher in a large wind power plant; values on the order of 5% of the wind turbine hub height are reported. These high values are rather extreme, and are expected to be valid only at some height above the rotorplane; in fact, the height of the rotorplane is a region of transition, between the lower values near the ocean surface and higher values above. A value of 0.01 m is in between, on a logarithmic scale, being representative of "flat grassy plains" [4]. This value is used for the analyses in the present report. Figure 1 through Figure 3 show the consequences of the selected surface roughness length, and the associated turbulence length scale.

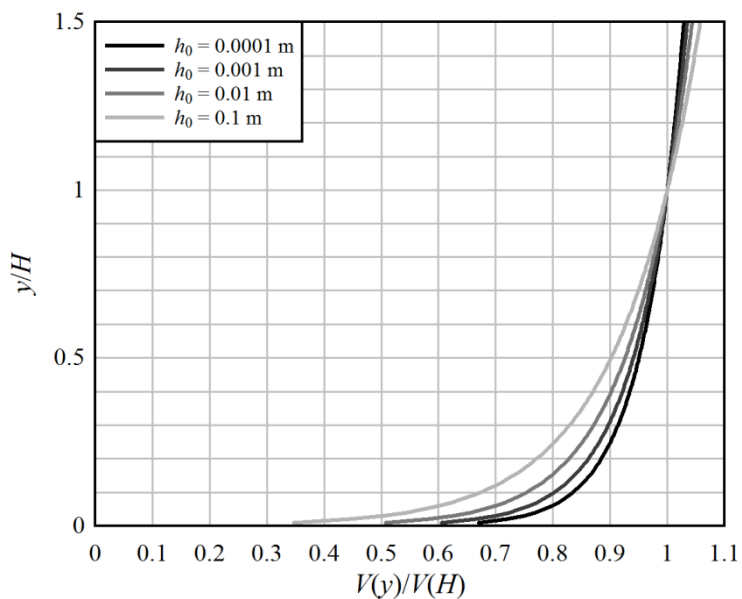


Figure 1: Profiles of windspeed with height for different values of surface roughness length. Here y indicates the elevation over the surface.

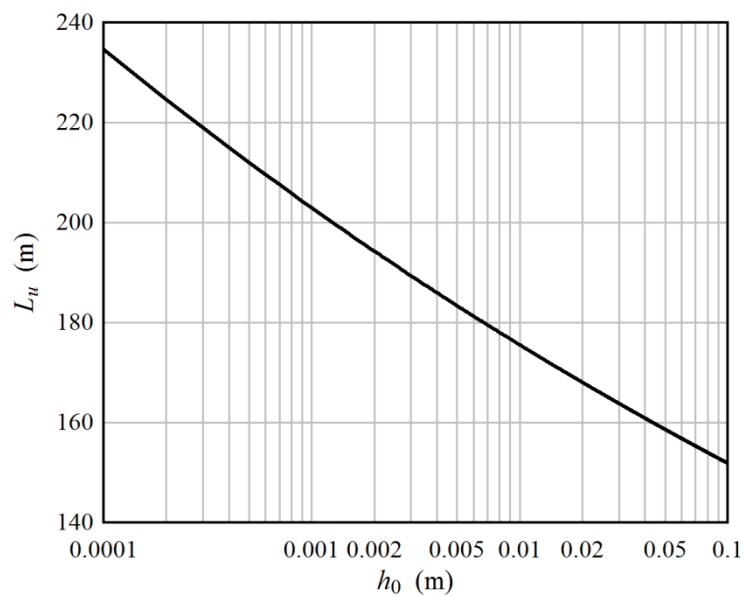


Figure 2: Turbulence length scale as a function of surface roughness length.

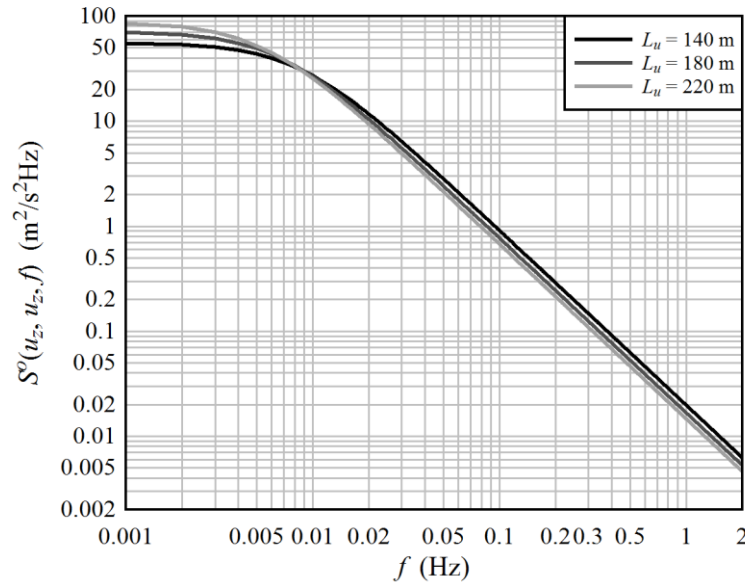


Figure 3: The von Karman turbulence spectrum, as a function of frequency and length scale. Shown for a windspeed of 10 m/s and turbulence intensity of 0.10.

2.2 Correlations in Space and Time

The inverse Fourier transform of Equation 2.2 is⁽¹⁾

$$Q_{zz}(0, \tau) = \frac{2\sigma_u^2}{\Gamma(1/3)} \left(\frac{V_\infty \tau}{2.68L_u} \right) K_{1/3} \left(\frac{V_\infty \tau}{1.34L_u} \right), \quad (2.4)$$

where by definition

$$Q_{ij}(s, \tau) := E[u_i(r, t)u_j(r + s, t + \tau)]. \quad (2.5)$$

Assuming that the turbulence is frozen, the distance $V_\infty \tau$ is synonymous with the z coordinate, and Equation 2.4 can be restated as

$$Q_{zz}(z, 0) = \frac{2\sigma_u^2}{\Gamma(1/3)} \left(\frac{z}{2.68L_u} \right)^{1/3} K_{1/3} \left(\frac{z}{1.34L_u} \right). \quad (2.6)$$

Its derivative is⁽²⁾

$$\frac{dQ_{zz}(z, 0)}{dz} = - \left(\frac{2\sigma_u^2}{\Gamma(1/3)} \right) \left(\frac{1}{1.34L_u} \right) \left(\frac{z}{2.68L_u} \right)^{1/3} K_{-2/3} \left(\frac{z}{1.34L_u} \right). \quad (2.7)$$

Following Davidson [10], for isotropic turbulence, the spatial correlation of turbulence velocity between any two points can be written as

$$Q_{ii}(s, 0) = Q_{ss}(s, 0) + \frac{s}{2} \frac{dQ_{ss}(s, 0)}{ds} - \frac{s_i^2}{2s} \frac{dQ_{ss}(s, 0)}{ds} \quad (2.8)$$

for velocity components in the same direction, and

¹ Connell [9], Kristensen and Frandsen [22]. $E[]$ is the expected value operator, K is the modified Bessel function of the second kind, r is an arbitrary coordinate, and u is the turbulent component of the wind.

² For instance, Merz [27]

$$Q_{ij}(s, 0) = -\frac{s_i s_j}{2s} \frac{dQ_{ss}(s, 0)}{ds} \quad (2.9)$$

for orthogonal components. Here z has been replaced with a generic coordinate s , since by isotropy Equations 2.8 and 2.9 apply in any direction and any coordinate frame. With these equations we can determine, in closed-form, the correlations between arbitrary components of turbulence at arbitrary locations in space. The key concept is now to formulate the desired correlations across space and time in terms of correlations across only space, taking advantage of the frozen turbulence assumption.

The relevant geometry is sketched in Figure 4. It is desired to relate the axial and tangential components of turbulence, u_z and u_t , at points A (radius r_1 and time t) and B (radius r_2 and time $t + \tau$) on the rotating blades. (Spanwise components are neglected.) By the assumption of frozen turbulence, this is equivalent to relating u_z and u_t at points A and S at time t , where S lies a distance $s_z = V_\infty \tau$ upwind of point B .

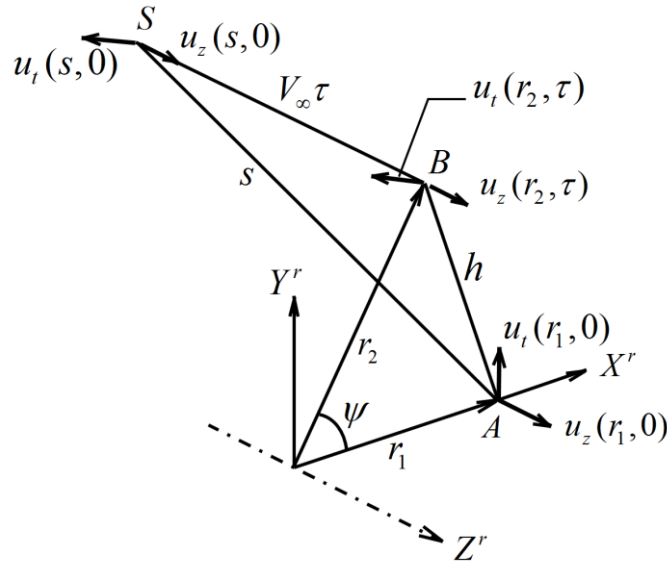


Figure 4: A sketch of the geometry for the rotationally-sampled turbulence problem.

It is emphasised that although Figure 4 is drawn, and the equations formulated, such that $\psi = 0$ at time t , the resulting correlations are valid for any angle about the azimuth. Also, the time t is arbitrary, and may be set to zero.

For points on the same blade,

$$s_x = r_2 \cos \psi - r_1; \quad s_y = r_2 \sin \psi. \quad (2.10)$$

For points on different blades, the equations are identical, except that ψ is replaced with $\psi + \psi_b$, ψ_b being the angular separation between the blades. Substituting these into Equations 2.8 and 2.9,

with $s = \sqrt{s_x^2 + s_y^2 + s_z^2}$ and $\psi = \Omega \tau$, the correlation components Q_{xx} , $Q_{xy} = Q_{yx}$, $Q_{xz} = Q_{zx}$, Q_{yy} , $Q_{yz} = Q_{zy}$, and Q_{zz} are obtained. Then,

$$Q_{zz}(r_1, r_2, \tau) = Q_{zz}(s, 0) \quad (2.11)$$

$$Q_{tt}(r_1, r_2, \tau) = -Q_{yx}(s, 0) \sin(\Omega \tau + \psi_b) + Q_{yy}(s, 0) \cos(\Omega \tau + \psi_b) \quad (2.12)$$

$$Q_{zt}(r_1, r_2, \tau) = -Q_{zx}(s, 0) \sin(\Omega\tau + \psi_b) + Q_{zy}(s, 0) \cos(\Omega\tau + \psi_b) \quad (2.13)$$

and

$$Q_{tz}(r_1, r_2, \tau) = Q_{yz}(s, 0). \quad (2.14)$$

The rotationally-sampled spectra are found by taking the FFT of Q_{zz} and Equations 2.11 through 2.14. Defining the Fourier transform pair

$$S(f) = \int_{-\infty}^{\infty} Q(\tau) \exp(-i2\pi f\tau) d\tau; \quad Q(\tau) = \int_{-\infty}^{\infty} S(f) \exp(i2\pi f\tau) df; \quad (2.15)$$

these can be put into FFT form,

$$S(k\Delta f) = \frac{1}{N\Delta f} \sum_{m=-(N/2-1)}^{N/2} Q(m\Delta\tau) \exp\left(\frac{-i2\pi km}{N}\right) \quad (2.16)$$

and

$$Q(m\Delta\tau) = \Delta f \sum_{k=-(N/2-1)}^{N/2} S(k\Delta f) \exp\left(\frac{i2\pi km}{N}\right). \quad (2.17)$$

As an example, Figure 5 and Figure 6 show the correlations between rotationally-sampled turbulence components at an outboard blade element, between outboard and inboard blade elements, and from one blade to the next. A given point on the blade sees turbulence as a heightened correlation at integer multiples of the rotational period, and a lack of correlation at half-periods. Note that $Q_{ii}(r_1, r_1, 0) = \sigma_u^2$, as expected.

The fluctuations of the tangential (in-plane) component are especially severe, as low-frequency yaw and tilt offsets in the wind direction, due to large-scale turbulent eddies, are seen by the blades as a sinusoidally-alternating component in the windspeed. This deserves particular emphasis, since previous frequency-domain turbulence models, such as that described by Burton *et al.* [4], have neglected the tangential component.

Figure 7 and Figure 8 show the spectra which are the Fourier transforms of Figure 5 and Figure 6, respectively. Multiples of the rotational frequency are evident.

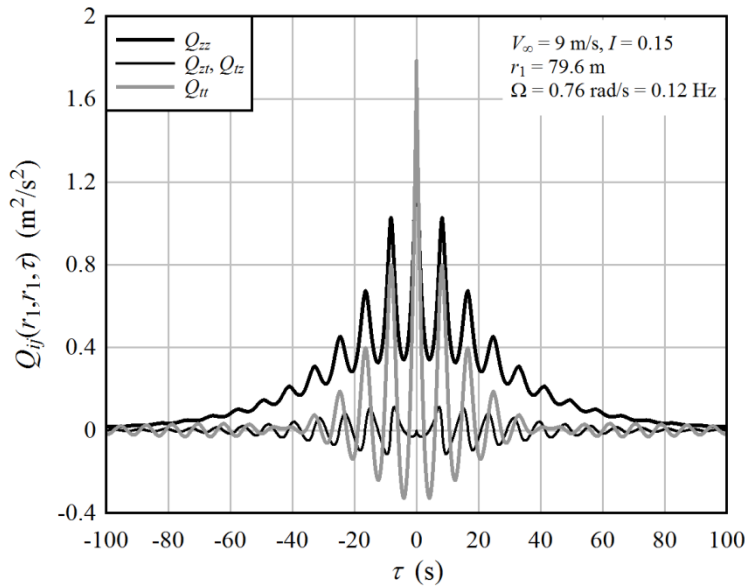


Figure 5: Auto- and cross-correlations between turbulence components at an outboard blade element.

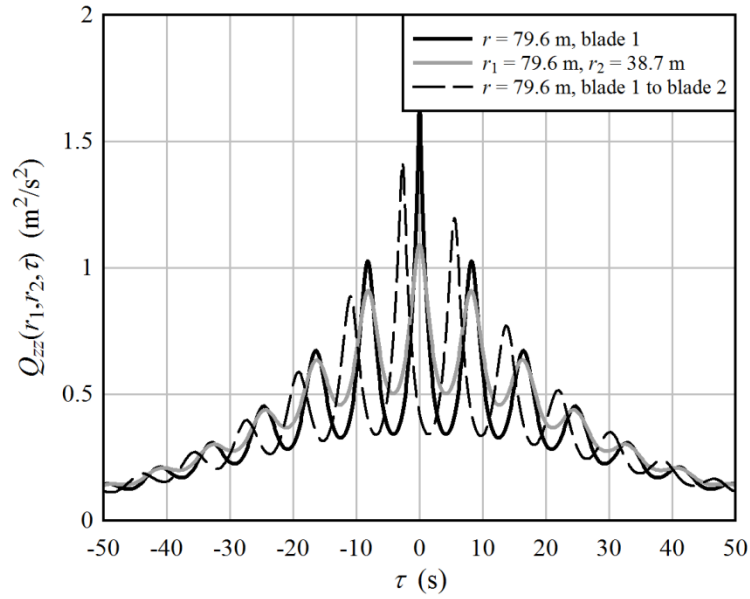


Figure 6: Z' -component correlation functions. The flow conditions are the same as those in Figure 5. Note the phase offset of the blade-to-blade correlation.

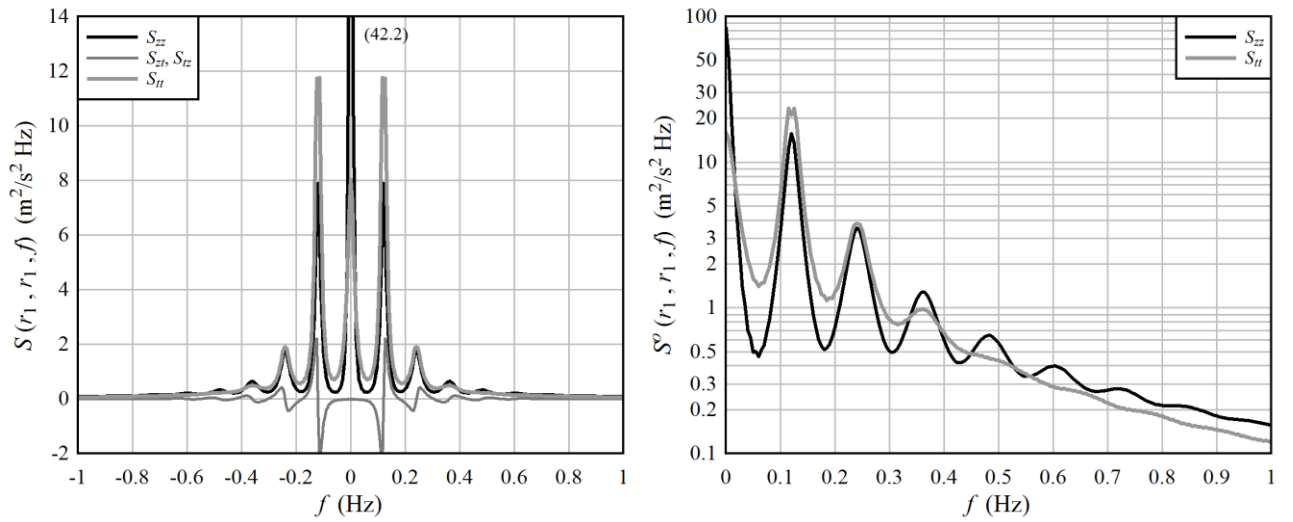


Figure 7: Turbulence spectra seen by a single point near the blade tip. The flow conditions are the same as those in Figure 5. At left: two-sided auto- and cross-spectra of the axial and tangential turbulence components. At right: one-sided auto-spectra of the axial and tangential turbulence components, plotted on a logarithmic scale.

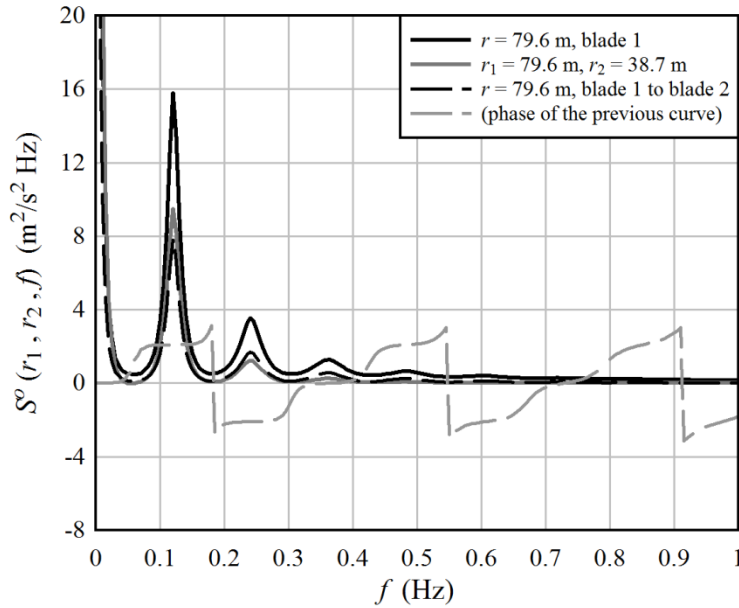


Figure 8: One-sided Z' -component turbulence spectra. The flow conditions are the same as those in Figure 5. The spectrum from a point on blade 1 to a point on blade 2 is complex, as expected based on the asymmetric correlation function.

2.3 Correlations in Multi-Blade Coordinates

In multi-blade coordinates, the correlations we seek are between the collective, cosine, and sine components. These are obtained from the physical components by the multi-blade coordinate transform, which itself is a function of the azimuth angle, and hence the time offset τ . The multi-blade coordinate transform is described by Coleman and Feingold [8], with wind turbine applications illustrated by Hansen [17], Bir [2], Stol [34], and Merz [29].

Consider first the correlation associated with two of the collective components,

$$Q_{00}^w(r_1, r_2, \tau) := E[u_0^w(r_1, t)u_0^w(r_2, t + \tau)] \quad (2.18)$$

This can be expressed in terms of physical coordinates:

$$Q_{00}^w(r_1, r_2, \tau) = E \left[\frac{1}{3} (u_1(r_1, t) + u_2(r_1, t) + u_3(r_1, t)) \right. \\ \left. \times \frac{1}{3} (u_1(r_2, t + \tau) + u_2(r_2, t + \tau) + u_3(r_2, t + \tau)) \right] \quad (2.19)$$

such that

$$Q_{00}^w(r_1, r_2, \tau) = \frac{1}{9} \left[Q_{ij}(s_{11}, 0) + Q_{ij}(s_{12}, 0) + Q_{ij}(s_{13}, 0) + Q_{ij}(s_{21}, 0) + Q_{ij}(s_{22}, 0) \right. \\ \left. + Q_{ij}(s_{23}, 0) + Q_{ij}(s_{31}, 0) + Q_{ij}(s_{32}, 0) + Q_{ij}(s_{33}, 0) \right]. \quad (2.20)$$

Here the i and j subscripts are either z or t , and the subscripts on the s terms indicate that the vector is to be taken from r_1 on the blade indicated by the first subscript, to r_2 on the blade indicated by the second subscript.

Next consider the correlation associated with two of the cosine components,

$$Q_{cc}^w(r_1, r_2, \tau) := E[u_c^w(r_1, t)u_c^w(r_2, t + \tau)]. \quad (2.21)$$

This time,

$$\begin{aligned} Q_{cc}^{\psi}(r_1, r_2, \tau) = E & \left[\frac{2}{3} (u_1 \cos \Psi_1(0) + u_2 \cos \Psi_2(0) + u_3 \cos \Psi_3(0)) \right. \\ & \times \left. \frac{2}{3} (u_1 \cos \Psi_1(\tau) + u_2 \cos \Psi_2(\tau) + u_3 \cos \Psi_3(\tau)) \right]. \end{aligned} \quad (2.22)$$

For brevity, we have introduced $\Psi_b := \psi + \psi_0 + \psi_b$, where ψ_0 may be used for averaging over the azimuth, and omitted (r_1, t) from the first three u terms and $(r_2, t + \tau)$ from the latter three u terms. It is not necessary to write out all the terms; the correlations in multi-blade coordinates can be written in matrix notation:

$$\mathbf{Q}^{\psi}(r_1, r_2, \tau) = \mathbf{T}_{B,p}^{\psi}(0) \mathbf{Q}_{ij}(s_{pq}(\tau), 0) [\mathbf{T}_{B,q}^{\psi}(\tau)]^T. \quad (2.23)$$

As before, i and j indicate the z and t components. The subscript p follows the row of \mathbf{Q}_{ij} , and q the column; refer to Equation 2.20.

Figure 9 plots an example of the turbulence correlations in multi-blade coordinates, for a radial location near the outer diameter of the rotor. Consider first the collective component, at upper left in the figure. This represents an average over the three blade elements, which are far apart, and together span nearly the diameter of the rotor. Thus, in comparison with Figure 5 for a single blade element, the sampling effect is much reduced. The frequency of sampling is increased from the rotational frequency 1P to the blade-passing frequency 3P. The same can be said for the tangential component of turbulence.

At upper right in Figure 9 are the turbulence correlations for the cosine-cosine and sine-sine multi-blade coordinates. These show a much more pronounced sampling effect, as each blade sweeps past the reference axis.

At bottom are the cross-correlations between the cosine and sine multi-blade coordinates. Although the magnitudes of the correlations are small, there is significant energy at the blade passing frequency. This is more clearly observed in Figure 10, which plots the S_{zz} and S_{tt} spectra associated with the correlations in Figure 9. Although the cosine-sine cross-spectra trend to zero as the frequency approaches zero, the spike at 3P is of a magnitude comparable to the collective, cosine-cosine, and sine-sine spectra.

The matrix of complex, multi-blade transformed, turbulence cross-spectra, between all the elements on the three blades, is the input to the frequency-domain aerodynamic loads analysis.

The present calculations are based on a constant rotor rotational speed. It would be useful to be able to estimate the rotationally-sampled turbulence spectra in the case where the rotational speed varies stochastically, in response to the wind and (linearized) control actions. This is suggested as a topic for future development.

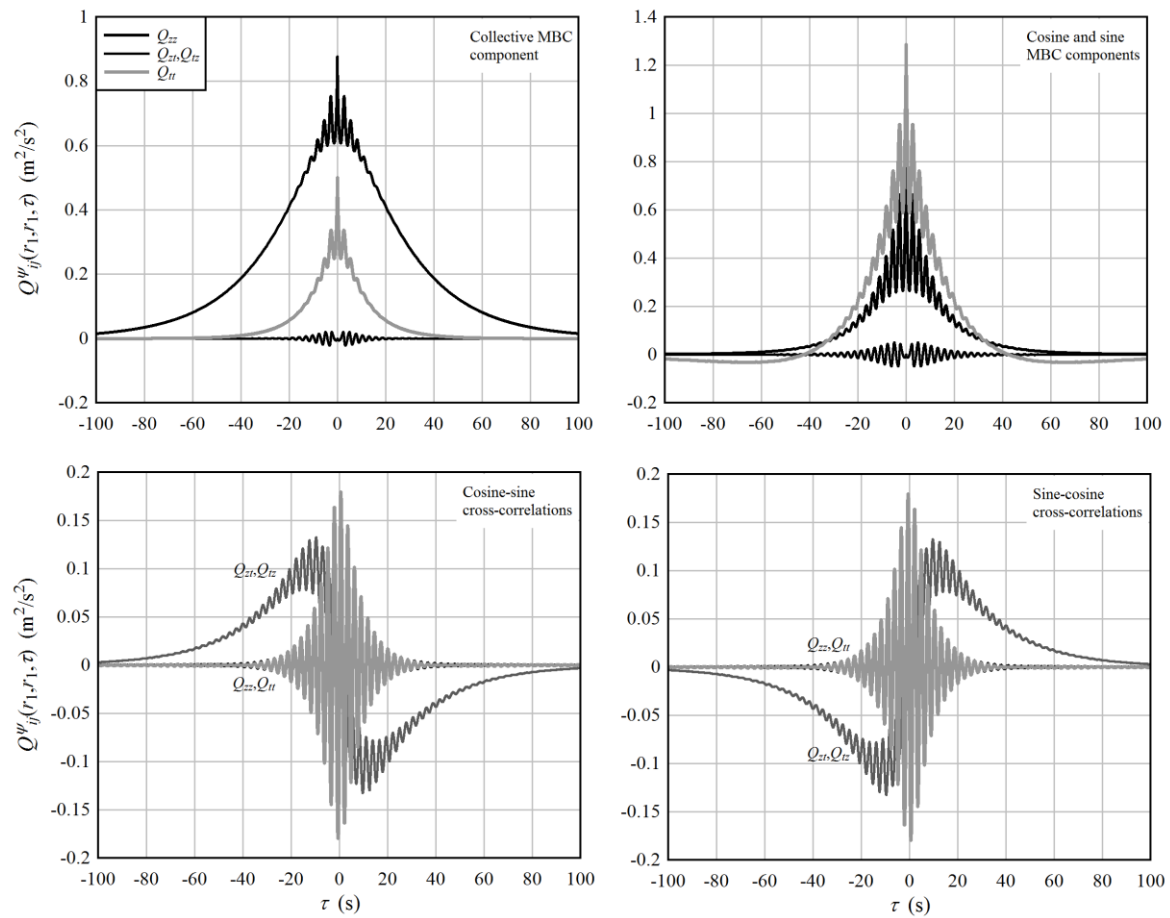


Figure 9: Turbulence correlations, in multi-blade coordinates, at a radial coordinate near the outer diameter of the rotor. Flow conditions and radial position are the same as those in Figure 5.

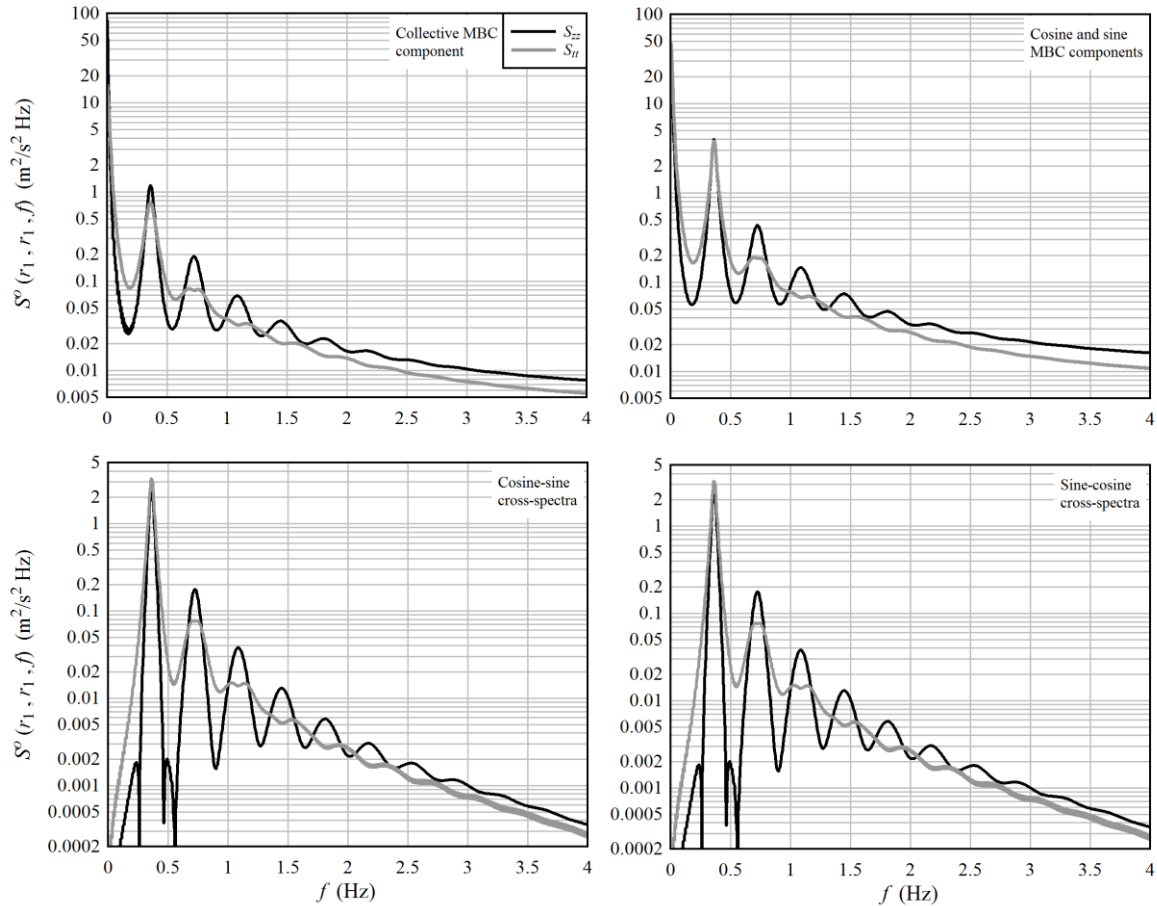


Figure 10: Turbulence spectra, in multi-blade coordinates, at a radial coordinate near the outer diameter of the rotor. Flow conditions and radial position are the same as those in Figure 5.

3 Wave Loads

The majority of energy in ocean waves is contained in a frequency band between 0.05 and 0.25 Hz. Exactly how the energy is distributed in this frequency band depends on the wave climate, characterized by a spectrum of wave height which is typically formulated as a function of the significant wave height H_s and wave period at the spectral peak T_p [11].

The oscillation of a wind turbine tower may be poorly damped – in particular in the side-to-side (orthogonal to the wind) mode, or when the rotor is parked – and so the transfer functions between wave loading and tower motion show sharp spikes at the resonance frequencies. As a consequence of the low damping, small amounts of energy in the wave loads in the vicinity of the resonance frequencies will give a disproportionately severe response. The first fore-aft and side-to-side natural frequencies of a utility-scale offshore wind turbine may fall within the range of 0.20 to 0.25 Hz.⁽³⁾ This means that the loads from relatively low-amplitude, short-period waves are of

³ A 10 MW wind turbine atop a monopile foundation, designed by L. Eliassen (Statkraft/NTNU), was found to have the first tower resonance frequencies in the vicinity of 0.21 to 0.24 Hz, depending on the assumptions made about the seabed conditions. This frequency comparison is reported in Section 5 of Merz [29].

concern. Also, it is important to consider second-order effects, which include the sums of pairs of frequencies across the wave spectrum and thus influence the energy content at frequencies above the nominal wave band. Second-order effects are present in the fluid drag term, which is proportional to $v|v|$, with v being the fluid velocity; the relationship between the local fluid velocity and pressure acting on a submerged body; the varying elevation of the ocean surface, with the corresponding variation in pressure on the structure; and in the shape of the wave profiles, including the relation between wave elevation and flow velocity and acceleration.

A variety of methods exist for computing second-order fluid drag spectra. For instance, Eatock Taylor and Rajagopalan ([13],[14]) apply a perturbation analysis to the fluid drag term, retaining terms to second order. Gudmestad and Connor [16] expand the drag term as a power series in the fluid velocity, retaining up to cubic terms; however, linear wave kinematics are assumed. In the former case, the load spectra are formulated as sums of cross-spectra between terms of various orders, and in the latter case, as nested convolutions of first-order spectra.

The wave loads on wind turbine monopiles, which may have diameters on the order of 10 m, are dominated by the inertia (fluid acceleration) forces. Drag is secondary. Herfjord and Nielsen [19] provide a method for computing second-order wave inertia forces on a monopile. They argue that the second-order potential can be neglected: the most important second-order terms are those related to the fluctuation in the surface elevation, and the velocity-squared term in Bernoulli's equation, both of which are second-order functions of the first-order potential. This is desirable, since the first-order potential, as derived by MacCamy and Fuchs [24], is readily computed. Full solutions for the second-order wave inertia forces are also available, for instance Chakrabarti [6] and Kim [21].

As input to the frequency-domain analysis we desire a matrix of the auto- and cross-spectra of wave loads at various elevations on the foundation. As with the wind loads, it is convenient to compute and store the spectral matrix upfront, rather than computing it anew with each analysis. Since the computation is to be performed upfront, it is feasible to compute one or more realizations of the nonlinear wave forces in the time domain, and subsequently compute the cross-correlations and cross-spectra numerically. This allows us to avoid higher-order spectral formulations.

Advanced analysis tools are available commercially for the computation of wave loads in the time domain. Such tools can be used to generate nodal force spectra, in the manner described herein. It is not within the present scope of the STAS program to implement a state-of-the-art calculation; we seek a basic method that is compatible in principle with the simplifying assumptions made elsewhere in the analysis. For fatigue calculations, it is common⁽⁴⁾ to use the Morison equation, with first-order wave kinematics in combination with Wheeler stretching [41]. However, for piles on the order of 10 m diameter, diffraction effects become important. The present approach thus combines the full first-order potential theory with Wheeler stretching and Morison drag. As shown in Section 3.5, this provides the same results as the Morison equation for small-diameter piles, and adds at least a partial consideration of free-surface effects to MacCamy and Fuchs' theory for large-diameter piles.

3.1 Wave Climate

A short-term wave climate is specified by a single-point amplitude spectrum, which is typically characterized by two parameters, a significant wave height H_s and a characteristic wave period T_p . The long-term wave climate at a given site is specified by discretizing the possible values of H_s and T_p into bins, and assigning a probability to each bin.

⁴ For instance, Chakrabarti [7].

3.1.1 Joint Probabilities of H_s and T_p

Fischer *et al.* [15] provide a thorough description of the climate conditions in the North Sea, including the three-way joint probability of H_s , T_p , and the windspeed V_∞ . Table I provides an example of the joint probabilities of H_s and T_p , for a location representative of the English sector of the North Sea, with 30 m water depth.

Table I: A scatter diagram: probabilities that H_s and T_p will fall within the given bins. Representative of the English sector of the North Sea, at 30 m water depth. These values can be compared with for instance Fischer *et al.* [15]. This table is intended for fatigue analysis; the resolution is not sufficient to predict lifetime extreme waves.

		T_p (s)							
		2	4	6	8	10	12	14	16
H_s (m)	1	0.0004	0.1397	0.2705	0.1261	0.0347	0.0075	0.0015	0.0003
	2	0.0000	0.0050	0.0998	0.1149	0.0428	0.0092	0.0015	0.0002
	3	0.0000	0.0000	0.0090	0.0473	0.0306	0.0071	0.0010	0.0000
	4	0.0000	0.0000	0.0002	0.0101	0.0181	0.0060	0.0007	0.0000
	5	0.0000	0.0000	0.0000	0.0006	0.0063	0.0039	0.0005	0.0000
	6	0.0000	0.0000	0.0000	0.0000	0.0010	0.0020	0.0004	0.0000
	7	0.0000	0.0000	0.0000	0.0000	0.0001	0.0006	0.0003	0.0000
	8	0.0000	0.0000	0.0000	0.0000	0.0000	0.0000	0.0001	0.0000

3.1.2 Wave Amplitude Spectra

For a given H_s and T_p , the spectrum of wave amplitude at a given, fixed point can be computed by one of several empirical formulas. The DNV version of the JONSWAP spectrum [11] is employed in the present analysis.

Realizations of wave time series with the given spectral properties can be created by dividing the spectrum into frequency bins of width Δf , and associating each frequency bin with a sinusoid of the appropriate amplitude, and random phase. That is, the elevation can be written

$$\zeta = \sum_{k=1}^N \zeta_{0,k} \cos(\omega_k t - k_k x + \epsilon_k) \quad (3.1)$$

with

$$\zeta_{0,k} = \sqrt{2S^o(f_k) \Delta f}, \quad (3.2)$$

$\omega_k = 2\pi f_k$, and ϵ_k is a random phase between 0 and 2π . $S^o(f_k)$ is the one-sided amplitude spectrum. The relationship between ω_k and k_k is given in the following section.

3.2 Wave Kinematics and First-Order Potential

Here the relationships between surface elevation and fluid displacement, velocity, and acceleration are established. The problem is formulated in terms of the velocity potential, a scalar field defined such that

$$\nabla \Phi := \mathbf{v}, \quad (3.3)$$

where \mathbf{v} is the velocity vector.

3.2.1 Incident Wave Potential

The incident wave potential Φ_I is that which exists when the structure is not present. Because linear superposition applies, we can consider a wave of a single frequency ω .

The incident wave potential obeys the Laplace equation. Working in cylindrical coordinates, this is

$$\frac{\partial^2 \Phi_I}{\partial r^2} + \frac{1}{r} \frac{\partial \Phi_I}{\partial r} + \frac{1}{r^2} \frac{\partial^2 \Phi_I}{\partial \theta^2} + \frac{\partial^2 \Phi_I}{\partial z^2} = 0 \quad (3.4)$$

The potential must be continuous in θ , such that

$$\Phi_I(r, \theta, z, t) = \Phi_I(r, \theta + 2\pi, z, t). \quad (3.5)$$

There is no flow through the sea floor:

$$\frac{\partial \Phi_I}{\partial z} = 0 \quad \text{at } z = -d. \quad (3.6)$$

The wave is assumed to be propagating in the $x = r \cos \theta$ direction. The phase of the surface elevation ζ is chosen such that the elevation is a maximum at $t = 0$ and $x = 0$. This leads to an expression for the surface elevation⁽⁵⁾

$$\zeta = \zeta_0 \Re \{ \exp[i(\omega t - kr \cos \theta)] \} \quad (3.7)$$

where ζ_0 is the amplitude of the wave. The kinematic and dynamic free-surface conditions are

$$\frac{\partial \Phi_I}{\partial z} - \frac{\partial \zeta}{\partial t} = 0 \quad \text{at } z = 0 \quad (3.8)$$

and

$$g\zeta + \frac{\partial \Phi_I}{\partial t} = 0 \quad \text{at } z = 0. \quad (3.9)$$

The surface elevation can be eliminated by taking the time derivative of Equation 3.9 and substituting into Equation 3.8. The result is

$$\frac{\partial \Phi_I}{\partial z} + \frac{1}{g} \frac{\partial^2 \Phi_I}{\partial t^2} = 0 \quad \text{at } z = 0. \quad (3.10)$$

Note that either free-surface boundary condition can be used to determine the correct phase of the velocity potential with respect to the surface elevation. Using the kinematic free-surface condition evaluated at $z = 0$ and $r = 0$,

$$f(\theta) \tau(t) = i\zeta_0 \omega \exp(i\omega t) \quad (3.11)$$

where $f(\theta)$ and $\tau(t)$ are respectively the azimuthal and time dependence of Φ_I . Thus the time dependence of Φ_I is $\Re \{ i \exp(i\omega t) \}$; in other words, Φ_I leads the surface elevation by 90° . The assumption that the wave is propagating in the x direction also leads to another condition on Φ_I , namely symmetry about the XZ plane:

$$\Phi_I(r, \theta, z, t) = \Phi_I(r, -\theta, z, t). \quad (3.12)$$

The Laplace equation can be solved by the separation of variables. Define $\Phi_I = P_I(r) \Theta_I(\theta) Z_I(z) [i \exp(i\omega t)]$ and substitute into Equation 3.4:

⁵ Different authors use different definitions of the phase of the surface elevation. This results in subtly different equations throughout. Of course, when corrected for the phase, the solutions must be the same.

$$\Theta_l Z_l \frac{d^2 P_l}{dr^2} + \Theta_l Z_l \frac{1}{r} \frac{dP_l}{dr} + P_l Z_l \frac{1}{r^2} \frac{d^2 \Theta_l}{d\theta^2} + P_l \Theta_l \frac{d^2 Z_l}{dz^2} = 0. \quad (3.13)$$

(Note that there are other solutions to the Laplace equation than those derived below. Here functions of alternate forms do not obey the radiation condition, and thus are omitted upfront.) The time dependence, $i \exp(i\omega t)$, immediately cancels out. Next, divide through by $P_l \Theta_l Z_l$:

$$\frac{1}{P_l} \frac{d^2 P_l}{dr^2} + \frac{1}{r P_l} \frac{dP_l}{dr} + \frac{1}{r^2 \Theta_l} \frac{d^2 \Theta_l}{d\theta^2} + \frac{1}{Z_l} \frac{d^2 Z_l}{dz^2} = 0. \quad (3.14)$$

For this to be true for all (r, θ, z) , it must be the case that

$$\frac{1}{Z_l} \frac{d^2 Z_l}{dz^2} = q_r^2, \quad (3.15)$$

and

$$\frac{1}{P_l} \frac{d^2 P_l}{dr^2} + \frac{1}{r P_l} \frac{dP_l}{dr} + \frac{1}{r^2 \Theta_l} \frac{d^2 \Theta_l}{d\theta^2} = -q_r^2, \quad (3.16)$$

where q_r is some constant, in general complex, and the exponent of 2 has been chosen for convenience. Furthermore, it must be the case that

$$\frac{1}{\Theta_l} \frac{d^2 \Theta_l}{d\theta^2} = -q_\theta^2, \quad (3.17)$$

where q_θ is some (perhaps complex) constant, and correspondingly

$$\frac{r^2}{P_l} \frac{d^2 P_l}{dr^2} + \frac{r}{P_l} \frac{dP_l}{dr} + r^2 q_r^2 - q_\theta^2 = 0. \quad (3.18)$$

Equation 3.15 has a solution of the form

$$Z_l = \gamma_1 \exp(q_r z) + \gamma_2 \exp(-q_r z). \quad (3.19)$$

The constants γ_1 and γ_2 may in general be complex. Applying the sea floor boundary condition,

$$\frac{dZ_l}{dz} = 0 \quad \text{at} \quad z = -d, \quad (3.20)$$

we obtain

$$\gamma_1 = \gamma_2 \exp(2q_r d); \quad Z_l = \gamma_2 [\exp(q_r(z+d)) + \exp(-q_r(z+d))]. \quad (3.21)$$

Applying the free surface boundary condition then gives:

$$\frac{dZ_l(0)}{dz} i \exp(i\omega t) - \frac{\omega^2}{g} Z_l(0) i \exp(i\omega t) = 0, \quad (3.22)$$

thus

$$q_r \frac{\exp(q_r d) - \exp(-q_r d)}{\exp(q_r d) + \exp(-q_r d)} = \frac{\omega^2}{g}. \quad (3.23)$$

If $q_r = k_r$ is real, the ratio of exponential functions will be $\tanh k_r d$. If $q_r = ik_r$ is imaginary, it will be $i \tan k_r d$. We must look at the radial function in order to say which is the case; but it will turn out that $q_r = k_r$ is real, and has a value which satisfies

$$k_r \tanh k_r d = \frac{\omega^2}{g}. \quad (3.24)$$

This also means that Z_I has the form

$$Z_I = \gamma_2 \cosh k_r (z + d), \quad (3.25)$$

where a factor of 2 has been incorporated into the constant γ_2 .

Next, consider the azimuthal function, satisfying Equation 3.17. The solution is of the form

$$\Theta_I = \gamma_3 \exp(iq_\theta \theta) + \gamma_4 \exp(-iq_\theta \theta). \quad (3.26)$$

The condition of continuity about the azimuth, Equation 3.5, requires that $q_\theta = m$ is a real integer, such that Θ_I consists of trigonometric functions which are periodic about the azimuth. The condition of symmetry, Equation 3.12, then gives

$$\gamma_3 \exp(im\theta) + \gamma_4 \exp(-im\theta) = \gamma_3 \exp(-im\theta) + \gamma_4 \exp(im\theta), \quad (3.27)$$

so

$$\gamma_3 = \gamma_4. \quad (3.28)$$

Therefore, the azimuthal solution takes the form

$$\Theta_I = \gamma_3 \cos m\theta \quad (3.29)$$

where a factor of 2 has been absorbed into γ_3 .

Finally, consider the radial function, Equation 3.18. By making a change of variables $s = q_r r$, with $ds = q_r dr$, the equation becomes

$$s^2 \frac{d^2 P_I}{ds^2} + s \frac{dP_I}{ds} + (s^2 - m^2)P_I = 0. \quad (3.30)$$

One can then assume a power series solution of the form

$$P_I = \sum_{j=0}^{\infty} a_j s^{j+n}. \quad (3.31)$$

Substituting into Equation 3.27 gives, after much algebra

$$P_I = \gamma_5 J_m(q_r r) + \gamma_6 Y_m(q_r r), \quad (3.32)$$

where J and Y denote Bessel functions of the first and second kind. If $q_r = ik_r$ is imaginary, it is customary to write

$$P_I = \gamma_5 I_m(k_r r) + \gamma_6 K_m(k_r r), \quad (3.33)$$

where complex constant factors have been absorbed into γ_5 and γ_6 . However, it is a property of Bessel functions that $Y_m(x) \rightarrow \infty$ as $x \rightarrow 0$, $K_m(x) \rightarrow \infty$ as $x \rightarrow 0$, and $I_m(x) \rightarrow \infty$ as $x \rightarrow \infty$. It is unphysical to have an unbounded velocity potential; therefore the only viable form of the radial function has $q_r = k_r$ a real number, and $\gamma_6 = 0$. This gives

$$P_I = \gamma_5 J_m(k_r r), \quad (3.34)$$

and establishes that Equation 3.24 is indeed the correct criterion for k_r .

The form of the velocity potential is now known to within a complex constant A_m :

$$\Phi_I = i \exp(i\omega t) \sum_{m=0}^{\infty} A_m J_m(k_r r) \cosh k_r (z + d) \cos m\theta, \quad (3.35)$$

where the index m denotes solutions associated with the different azimuthal functions $\cos m\theta$. (One could also write the sum from $m = -\infty$ to $m = \infty$. It makes little difference; the solution then differs by a factor of 2 on all the terms $m \neq 0$. Compare Eatock Taylor and Hung [12] with Miles and Gilbert [30].)

To solve for the coefficients A_m , first employ the dynamic free-surface condition, Equation 3.9, using the expression for ζ given in Equation 3.1:

$$\frac{g\zeta_0}{\omega} \exp(-ik_r r \cos \theta) = \sum_{m=0}^{\infty} A_m J_m(k_r r) \cosh k_r d \cos m\theta. \quad (3.36)$$

(Note that the wave number k in Equation 3.1 is the same as the value of k_r which satisfies Equation 3.24.) Multiply both sides by $\cos n\theta$ and integrate from 0 to π :

$$\frac{g\zeta_0}{\omega} \int_0^{\pi} \cos n\theta \exp(-ik_r r \cos \theta) d\theta = \sum_{m=0}^{\infty} A_m J_m(k_r r) \cosh k_r d \int_0^{\pi} \cos n\theta \cos m\theta d\theta. \quad (3.37)$$

On the right-hand side of Equation 3.37, all the integral terms go to zero except for $m = n$. On the left-hand side, it is a property of Bessel functions that

$$J_n(z) = \frac{1}{(-i)^n \pi} \int_0^{\pi} \cos n\theta \exp(-iz \cos \theta) d\theta \quad (3.38)$$

for n an integer.⁽⁶⁾ Equation 3.37 then becomes

$$\frac{g\zeta_0}{\omega} (-i)^n \pi J_n(k_r r) = A_n J_n(k_r r) \cosh k_r d \int_0^{\pi} \cos^2 n\theta d\theta. \quad (3.39)$$

Noting that

$$\int_0^{\pi} \cos^2 n\theta d\theta = \begin{cases} \pi/2 & n \neq 0 \\ \pi & n = 0 \end{cases} \quad (3.40)$$

switching the arbitrary index from n back to m , and solving for A_m , the result is

$$A_m = \epsilon_m (-i)^m \frac{g\zeta_0}{\omega \cosh k_r d}, \quad (3.41)$$

where $\epsilon_m = 1$ for $m = 0$, and 2 otherwise. The incident potential is thus

$$\Phi_I = \frac{g\zeta_0}{\omega} \exp(i\omega t) \frac{\cosh k_r(z+d)}{\cosh k_r d} \sum_{m=0}^{\infty} i^{m+1} (-1)^m \epsilon_m J_m(k_r r) \cos m\theta. \quad (3.42)$$

3.2.2 Total Linear Potential

The total potential is composed of the incident potential plus the diffraction potential, $\Phi = \Phi_I + \Phi_d$, where the latter accounts for the alteration of the flow field due to the presence of the structure. In the present case, the structure is assumed to be a large, rigid cylinder, as sketched in Figure 11. If the foundation were a lattice structure, then this sort of potential solution would not be necessary, as the Morison equation is sufficient for sections of small diameter [11].

⁶ This follows from an identity given by Abramowitz and Stegun [1] p 360, where the sign on the exponential is changed by noting that $J_m(-z) = (-1)^m J_m(z)$ for integer m .

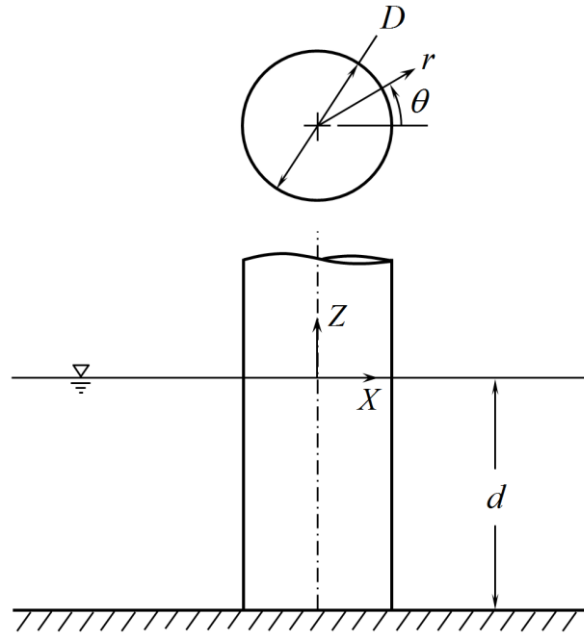


Figure 11: A cylinder in the ocean.

The diffraction potential satisfies the Laplace equation:

$$\frac{\partial^2 \Phi_d}{\partial r^2} + \frac{1}{r} \frac{\partial \Phi_d}{\partial r} + \frac{1}{r^2} \frac{\partial^2 \Phi_d}{\partial \theta^2} + \frac{\partial^2 \Phi_d}{\partial z^2} = 0 \quad (3.43)$$

The potential must be continuous in θ :

$$\Phi_d(r, \theta, z, t) = \Phi_d(r, \theta + 2\pi, z, t). \quad (3.44)$$

The potential must be symmetric about the XZ plane, due to the axisymmetry of the body and the assumption that the incident waves approach in the X direction:

$$\Phi_d(r, \theta, z, t) = \Phi_d(r, -\theta, z, t). \quad (3.45)$$

The kinematic and dynamic free-surface conditions apply:

$$\frac{\partial \Phi_d}{\partial z} - \frac{\partial \zeta}{\partial t} = 0; \quad g\zeta + \frac{\partial \Phi_d}{\partial t} = 0; \quad (3.46)$$

at $z = 0$. There can be no flow through the seabed:

$$\frac{\partial \Phi_d}{\partial z} = 0 \quad \text{at} \quad z = -d. \quad (3.47)$$

And there can be no flow through the cylinder:

$$\frac{\partial \Phi_d}{\partial r} + \frac{\partial \Phi_d}{\partial r} = 0 \quad \text{for} \quad r = \frac{D}{2} \quad \text{and} \quad -d < z \leq 0. \quad (3.48)$$

Finally, the outgoing diffracted waves must behave as

$$\Phi_d \propto \frac{1}{\sqrt{r}} \exp(-ikr) \quad \text{as} \quad r \rightarrow \infty. \quad (3.49)$$

(This is the "radiation condition", and can be derived from energy conservation. See for instance Newman [32].)

As in Section 3.2.1, the Laplace equation is solved by separation of variables, which leads to separate differential equations for $P_d(r)$, $\Theta_d(\theta)$, and $Z_d(z)$:

$$r^2 \frac{d^2 P_d}{dr^2} + r \frac{dP_d}{dr} + (r^2 q_r^2 - q_\theta^2) P_d = 0; \quad (3.50)$$

$$\frac{d^2 \Theta_d}{d\theta^2} + q_\theta^2 \Theta_d = 0; \quad (3.51)$$

$$\frac{d^2 Z_d}{dz^2} - q_r^2 Z_d = 0. \quad (3.52)$$

The boundary conditions on Θ_d are the same as those on Θ_I , so the solution will be of the same form:

$$\Theta_d = \gamma_3 \cos m\theta, \quad (3.53)$$

with $q_\theta = m$, an integer.

The boundary conditions on Z_d are also the same as those on Z_I , so it follows that the solution can be written

$$Z_d = \gamma_2 [\exp(q_r(z+d)) + \exp(-q_r(z+d))] \quad (3.54)$$

where q_r must satisfy

$$q_r \frac{\exp(q_r d) - \exp(-q_r d)}{\exp(q_r d) + \exp(-q_r d)} = \frac{\omega^2}{g}. \quad (3.55)$$

The domain for the diffraction potential does not include $r = 0$, therefore q_r is defined by all solutions of Equation 3.55. Thus when $q_r = k_r$ is real,

$$k_r \tanh k_r d = \frac{\omega^2}{g}. \quad (3.56)$$

Equation 3.56 has one solution. When $q_r = i\kappa$ is imaginary (with κ defined to be real),

$$\kappa \tan \kappa d = -\frac{\omega^2}{g}. \quad (3.57)$$

This has an infinite number of solutions.

The values of k_r and κ in Equations 3.56 and 3.57 are such that the Z functions are orthogonal over the depth, $d \leq z \leq 0$. (This is stated without proof.)

Solutions for the velocity potential Φ_d are either of the form:

$$\Phi_d = i \exp(i\omega t) [\gamma_5 J_m(k_r r) + \gamma_6 Y_m(k_r r)] \cosh k_r(z+d) \cos m\theta, \quad (3.58)$$

or of the form:

$$\Phi_d = i \exp(i\omega t) [\gamma_5 I_m(\kappa r) + \gamma_6 K_m(\kappa r)] \cos \kappa(z+d) \cos m\theta \quad (3.59)$$

The total solution is a linear combination of all the possible solutions. It is convenient to introduce an index n , defining $n = 0$ to represent the solution corresponding to k_r , and $n \geq 1$ representing sequential solutions κ_n of Equation 3.57. Then the total solution for Φ_d can be written as:

$$\Phi_d = i \exp(i\omega t) \sum_{m=0}^{\infty} \sum_{n=0}^{\infty} [A_{mn} P_{d,mn}(r) + \alpha_{mn} Q_{d,mn}(r)] Z_{d,n}(z) \cos m\theta, \quad (3.60)$$

with

$$P_{d,mn}(r) = \begin{cases} J_m(k_r r) & n = 0 \\ I_m(\kappa_n r) & n \neq 0 \end{cases}, \quad (3.61)$$

$$Q_{d,mn}(r) = \begin{cases} Y_m(k_r r) & n = 0 \\ K_m(\kappa_n r) & n \neq 0 \end{cases}, \quad (3.62)$$

and

$$Z_{d,n}(z) = \begin{cases} \cosh k_r(z+d) & n = 0 \\ \cos \kappa_n(z+d) & n \neq 0 \end{cases}. \quad (3.63)$$

Applying the radiation and cylinder-wall boundary conditions, Equations 3.48 and 3.49, gives the unknown coefficients A_{mn} and α_{mn} . The radiation condition must be satisfied as $r \rightarrow \infty$. Asymptotic forms of J and Y are [40]

$$J_m(k_r r) = \sqrt{\frac{2}{\pi k_r r}} \cos\left(k_r r - \frac{m\pi}{2} - \frac{\pi}{4}\right) \quad (3.64)$$

and

$$Y_m(k_r r) = \sqrt{\frac{2}{\pi k_r r}} \sin\left(k_r r - \frac{m\pi}{2} - \frac{\pi}{4}\right). \quad (3.65)$$

The correct asymptotic behavior is therefore attained by employing a radial function⁷

$$H_m^{(2)}(k_r r) := J_m(k_r r) - iY_m(k_r r), \quad (3.66)$$

The radiation condition also implies that $n = 0$ is the only feasible value for the diffraction potential. In other words,

$$\alpha_{m0} = -i A_{m0}, \quad \text{and} \quad A_{mn} = \alpha_{mn} = 0 \quad \text{for} \quad n > 0. \quad (3.67)$$

The cylinder wall boundary condition relates the diffraction and incident potentials. We have for the partial derivatives

$$\begin{aligned} \frac{\partial \Phi_I}{\partial r} &= \frac{g \zeta_0}{\omega} \exp(i\omega t) \frac{\cosh k_r(z+d)}{\cosh k_r d} \\ &\times \sum_{m=0}^{\infty} i^{m+1} (-1)^m \epsilon_m \left[-k_r J_{m+1}(k_r r) + \frac{m}{r} J_m(k_r r) \right] \cos m\theta \end{aligned} \quad (3.68)$$

and

$$\begin{aligned} \frac{\partial \Phi_d}{\partial r} &= i \exp(i\omega t) \cosh k_r(z+d) \\ &\times \sum_{m=0}^{\infty} A_{m0} \left[-k_r J_{m+1}(k_r r) + \frac{m}{r} J_m(k_r r) - i \left(-k_r Y_{m+1}(k_r r) + \frac{m}{r} Y_m(k_r r) \right) \right] \cos m\theta. \end{aligned} \quad (3.69)$$

⁷ Some sources employ $H_m^{(1)} := J_m + iY_m$. The difference is whether the travelling surface wave was defined with the convention $\exp[i(\omega t - kx)]$, as here, or $\exp[i(kx - \omega t)]$.

Letting $r = R := D/2$, and solving for the coefficients A_{m0} , accounting for the orthogonality of $\cos m\theta$, gives the result

$$A_{m0} = i^m (-1)^{m+1} \epsilon_m \frac{g \zeta_0}{\omega \cosh k_r d} \times \left[\frac{-k_r J_{m+1}(k_r R) + \frac{m}{R} J_m(k_r R)}{-k_r J_{m+1}(k_r R) + \frac{m}{R} J_m(k_r R) - i \left(-k_r Y_{m+1}(k_r R) + \frac{m}{R} Y_m(k_r R) \right)} \right]. \quad (3.70)$$

The velocity potential, for a single sinusoidal wave of a given frequency, is the sum of the incident and diffraction potentials:

$$\Phi = \frac{g \zeta_0}{\omega} \exp(i\omega t) \frac{\cosh k_r (z + d)}{\cosh k_r d} \times \sum_{m=0}^{\infty} i^{m+1} (-1)^m \epsilon_m \left(J_m(k_r r) - f_m(R) [J_m(k_r r) - i Y_m(k_r r)] \right) \cos m\theta, \quad (3.71)$$

where

$$f_m(R) := \frac{-k_r J_{m+1}(k_r R) + \frac{m}{R} J_m(k_r R)}{-k_r J_{m+1}(k_r R) + \frac{m}{R} J_m(k_r R) - i \left(-k_r Y_{m+1}(k_r R) + \frac{m}{R} Y_m(k_r R) \right)}. \quad (3.72)$$

The velocity potential is sinusoidal, at the incident wave frequency. In the cases encountered in the present analyses, it was observed that ten m terms was sufficient for convergence.

For computational purposes, the ratio of hyperbolic cosines is evaluated as

$$\frac{\cosh a}{\cosh b} = \frac{\exp(a - b) + \exp(-a - b)}{1 + \exp(-2b)}. \quad (3.73)$$

Equation 3.56 can be solved approximately for k_r as

$$k_r = \begin{cases} \frac{\sqrt{x} + p(x)}{d} & x < 5 \\ \frac{x}{d} & x \geq 5 \end{cases} \quad (3.74)$$

with

$$p(x) = 0.00052076133991x^5 - 0.00600002847615x^4 + 0.10996199804700x^3 + 0.12708453727900x^2 + 0.0670771673249x \quad (3.75)$$

and

$$x := \frac{d \omega^2}{g}. \quad (3.76)$$

In the real ocean, where the frequency content is spread over a range, and not just a single frequency, the total potential is obtained by superposing Equation 3.68 for each of a sequence of frequency bins. The appropriate wave amplitude $\zeta_{0,k}$ is determined for each wave by Equation 3.2, and the phase offset is introduced as $\exp[i(\omega_k t + \varepsilon_k)]$.

3.3 Pressure Forces

The fluid pressure forces on the surface of the cylinder can be computed from the velocity potential by Bernoulli's equation, which will be given shortly. First, though, it is worth taking a step back and considering the type of model on which the pressure forces will be applied, as this influences the strategy used to obtain a numerical solution.

Figure 12 shows a sketch of an offshore wind turbine, represented by finite beam elements whose nodes are shown as dots. The element distribution is refined in the vicinity of the waterline, in order to better and resolve the wave loads. Loads are applied to the model only at the nodes. Concentrated sources of loading which act in between nodes are assigned to the adjacent nodes by interpolation. Each node allows for six load components: F_x , F_y , F_z , M_x , M_y , and M_z . At present it is assumed that the waves progress along the X axis; then due to the symmetry of the configuration, the only net force is F_x . (F_y may also be nonzero when there is a misaligned ocean current, but its fluctuating component is small.) The restriction that waves progress along the X axis can be subsequently relaxed by applying coordinate transformations. We wish to compute the cross-spectra between the values of F_x at the nodes in the finite element model, in order to determine the spectral properties of the structural response.

Some references ([19],[24]) focus on the total, integrated forces on a pile, from the seabed to waterline. However, the present model requires the distribution, as a function of z coordinate, of the effective forces acting on the centerline of the cylinder, such that these can be interpolated as point loads at the nodes. If we consider the pressure p acting on an element of the cylinder surface dA' , as sketched in Figure 13, then by the axisymmetry of the cylinder this can be mapped to an identical force $p dA'$ acting at the same z' coordinate on the element axis.

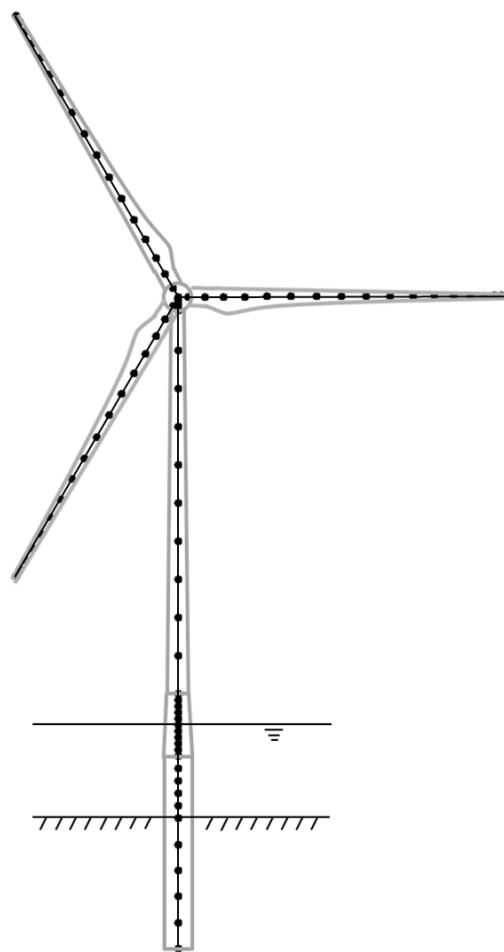


Figure 12: Sketch of an offshore wind turbine, showing a finite beam element representation. The element density is increased in the vicinity of the waterline, in order to increase the resolution of the applied wave loads.

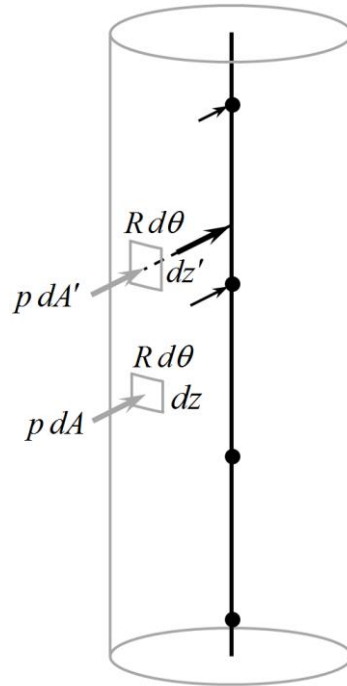


Figure 13: Mapping pressure forces from the location dA associated with the first-order potential, to a location dA' which accounts for the instantaneous elevation of the wave, to the beam element axis, and finally as equivalent point forces on the adjacent nodes. Note the difference in size between the elements dA and dA' which is a consequence of the stretching operation. The illustration shows the case where a wave crest is passing the element dA ; if it were a trough, the element dA' would be located below dA , and the length dz' would be compressed, rather than extended.

3.3.1 Bernoulli's Equation

Bernoulli's equation relates the velocity potential and pressure in the fluid:

$$\frac{d\Phi}{dt} + \frac{1}{2} |\nabla\Phi|^2 + \frac{p}{\rho} + gz = 0. \quad (3.77)$$

In a purely first-order calculation, such as MacCamy and Fuchs [24], the $|\nabla\Phi|^2$ term is neglected, and the total force can be determined in closed-form by integrating the pressure, evaluated at $r = R$, over θ and z .

Herfjord and Nielsen [19] investigate the forces to second order. They argue, based on the complete second-order potential solution by Chakrabarti, that the most important contribution to the second-order forces is made by the first-order potential, accounting for the instantaneous elevation of the free-surface, and the $|\nabla\Phi|^2$ term in Bernoulli's equation. The second-order potential has a smaller effect, and is neglected. This simplification seems appropriate for the present analysis, where the dynamic response of the wind turbine is linearized, and high precision is not warranted.

By the definition of the velocity potential, and applying the boundary condition at the cylinder surface,

$$|\nabla\Phi|^2 = v_\theta^2 + v_z^2 \quad \text{at} \quad r = R. \quad (3.78)$$

From Equation 3.71,

$$v_{\theta}|_{r=R} = \frac{1}{R} \frac{\partial \Phi}{\partial \theta} \Big|_{r=R} = \frac{g \zeta_0}{R \omega} \exp(i \omega t) \frac{\cosh k_r (z + d)}{\cosh k_r d} \times \sum_{m=0}^{\infty} i^{m+1} (-1)^{m+1} \epsilon_m \left(J_m(k_r R) - f_m(R) H_m^{(2)}(k_r R) \right) m \sin m \theta \quad (3.79)$$

and

$$v_z|_{r=R} = \frac{\partial \Phi}{\partial z} \Big|_{r=R} = k_r \frac{g \zeta_0}{\omega} \exp(i \omega t) \frac{\sinh k_r (z + d)}{\cosh k_r d} \times \sum_{m=0}^{\infty} i^{m+1} (-1)^m \epsilon_m \left(J_m(k_r R) - f_m(R) H_m^{(2)}(k_r R) \right) \cos m \theta. \quad (3.80)$$

Solving Equation 3.77 for the pressure,

$$p(R, \theta, z) = -\rho \frac{d\Phi}{dt} - \frac{1}{2} \rho (v_{\theta}^2 + v_z^2) - \rho g z. \quad (3.81)$$

Thus, while the fluid velocity is sinusoidal, at the incident wave frequency, and may be superposed, the pressure is not purely sinusoidal at the incident frequency, and may not be superposed.

Hertfjord and Nielsen consider a pair of sinusoidal waves with frequencies ω_1 and ω_2 , wavenumbers k_1 and k_2 , and phases ϵ_1 and ϵ_2 . They solve for the integral of the quadratic terms in Equation 3.81 over the depth and circumference of the cylinder, considering the interactions of the pair of waves. The total contribution of the quadratic terms can then be expressed as the sum of the contributions from all possible pairs, considering the decomposition of the wave elevation according to Equation 3.1. The integrals of the quadratic terms are carried only up to the mean free surface, which is valid to second order.

In the present implementation, especially in light of the surface-elevation effects in the following section, it makes sense to perform the integral numerically; that is, to discretize the cylinder surface into elements over which the flow parameters are assumed constant. The flow velocities v_{θ} and v_z can be computed directly by summing Equations 3.79 and 3.80, in the manner of Equation 3.1. Then Equation 3.81 can be evaluated directly to obtain the pressure, including the $|\nabla \Phi|^2$ term.

3.3.2 Surface-Elevation Effects

To first order, the velocity potential is evaluated up to the mean free surface. Hertfjord and Nielsen [19] account for the instantaneous elevation of the free surface by assuming that the velocity potential is constant, at its value at $z = 0$, between the mean free surface and the instantaneous free surface. The first-order force is then incremented by integrating the pressure, evaluated using the first-order velocity potential, up to (or down to) the instantaneous surface. This allows analytical expressions for the integrated force to be derived, accurate to second order. As was the case with the Bernoulli equation, the expressions are formulated for a generic pair of sinusoidal waves, with the total effect evaluated by considering all the permutations of pairs.

Wheeler [41] proposed an alternate, empirical method to account for the fluctuating surface elevation. In this approach, it is assumed that the first-order potential and velocity profiles, as a function of depth, are valid; but these profiles are "stretched" (or compressed) in the z coordinate such that they extend to the instantaneous free surface. The stretching function is

$$z + d = (z' + d) \frac{d}{d + \zeta}, \quad (3.82)$$

where z is the coordinate at which the first-order potential is to be evaluated, and z' is the physical coordinate. For $z' > \zeta$, of course, the fluid velocity and forces are zero. Note that

$$dz = dz' \frac{d}{d + \zeta}. \quad (3.83)$$

Thus, as sketched in Figure 13, the size of a differential element stretches or contracts as well.

In comparison with a strict second-order solution of the potential-flow problem, Wheeler stretching has the advantage that the empirical viscous drag force can be incorporated directly into the analysis. The Morison principle is employed, whereby the viscous drag force is simply added (with appropriate phase) to the potential solution. The drag coefficient is selected as $C_D = 1$ for analysis. (In Section 3.5, $C_D = 0.6$ is used for comparison with laboratory and field data collected on pristine cylinders). The flow velocity is taken as that at the centerline of the cylinder, computed as if the cylinder were not present.

To sum up, the present method can be considered an extension of the most basic feasible design approach, wherein the Morison equation is combined with linear wave kinematics and Wheeler stretching. Field and laboratory experiments ([3],[20],[37]) indicate that, for small cylinders, the basic Morison approach provides good estimates of cumulative load cycles under irregular wave conditions. However, extreme loads may be underpredicted.

The present method extends the basic Morison approach in two ways. First, the full linear potential-flow solution is used instead of an added mass coefficient. This means that the results are valid in the case where the cylinder diameter is on the same order as the wavelength. This may be important, since relatively low-amplitude, short-wavelength waves may approach the resonance frequency of the tower. In addition, the most important contributions to the sum-frequency effects – the free-surface elevation and the nonlinear terms in Bernoulli's equation – are included. The present method can therefore be used to study the excitation and damping of tower resonance, at frequencies which lie just above the nominal wave frequency band.

3.4 Load Spectra

The cylinder surface is discretized into areas dA of height dz and width $R d\theta$. The pressure is computed at the centerpoint of each elemental area, and is assumed to be constant over the element. Equation 3.81 is used; but the hydrostatic pressure is assumed to remain constant. (Near the free surface, the dynamic free-surface boundary condition

$$\frac{\partial \Phi}{\partial t} + g\zeta = 0, \quad (3.84)$$

when the profile is stretched, implicitly accounts for the hydrostatic pressure term.) The element z coordinate is then stretched to z' , and the area increased from dA to dA' , using Equations 3.82 and 3.83. The X (wave propagation direction) component of the force is extracted,

$$dF_x = -p dA' \cos \theta. \quad (3.85)$$

and this is distributed to the two adjacent nodes on the structural beam model, using linear weighting of the stretched z' coordinate. The summation of the contributions from all the cylinder surface elements gives the total nodal forces.

At the same time, the viscous drag force is computed in the manner of Morison's equation, for the section of the cylinder at elevation z . This is also stretched to z' and distributed to the adjacent nodes. Representing the flow about the cylinder with a single representative velocity is not valid when the diameter-to-wavelength ratio is large; however, in this case viscous drag is negligible, so it is acceptable to always include the drag term in the analysis.

The result is a time series of the effective hydrodynamic force at each node in the structural model. From this, cross-correlations are computed numerically:

$$Q_{jk}(\tau) := E[F_x(z_j, t)F_x(z_k, t + \tau)] = \frac{1}{T} \int_{-T/2}^{T/2} F_x(z_j, t)F_x(z_k, t + \tau) dt \quad (3.86)$$

or, in discrete form,

$$Q_{jk}(m\Delta\tau) = \frac{1}{N} \sum_{n=-(N/2-1)}^{N/2} F_x(z_j, n\Delta t) F_x(z_k, n\Delta t + m\Delta\tau). \quad (3.87)$$

This is computed numerically using fast Fourier transforms (FFT), by the procedure described by Press *et al.* [33]. FFTs are performed on the individual F_x time series:

$$\tilde{F}_x(z_j, m\Delta f) = \sum_{n=-(N/2-1)}^{N/2} F_x(z_j, n\Delta t) \exp\left(\frac{-i 2\pi n m}{N}\right) \quad (3.88)$$

Then, the cross-spectra are computed as

$$S_{jk}(m\Delta f) = \tilde{F}_x(z_k, m\Delta f) [\tilde{F}_x(z_j, m\Delta f)]^* \Delta f \quad (3.89)$$

and the cross-correlations are obtained by the inverse Fourier transform,

$$Q_{jk}(n\Delta\tau) = \frac{1}{N^2} \sum_{m=-(N/2-1)}^{N/2} \tilde{F}_x(z_k, m\Delta f) [\tilde{F}_x(z_j, m\Delta f)]^* \exp\left(\frac{i 2\pi n m}{N}\right). \quad (3.90)$$

3.5 Validation

Figure 14 compares the present method (pressure integration plus drag) with a standard Morison formulation. The geometry is taken from the Christchurch Bay field experiments, as reported by Najafian *et al.* [31]. The cylinder diameter is 0.48 m, and the "Level 3" section is 0.535 m long, mounted 2.41 m below the mean free surface. The water depth is 9.21 m. Loads on the Level 3 section were computed for a sinusoidal incident wave, with amplitude 1.4 m and period 4.5 s. This combination of geometry and wave state lies in a regime where it is expected that both inertia and drag are significant, and the Morison equation is valid. The present method indeed reproduces the forces obtained by the Morison equation. Wheeler stretching was applied in both cases.

Najafian *et al.* report the force spectra measured at the Level 3 section, together with the local water particle velocity spectra measured just upstream of the section. The water particle velocity spectra in the wave-frequency band are matched roughly using a two-peaked Ochi-Hubble spectrum [11], with $\lambda = 0.80$, $H_s = 0.95$ m, and $T_p = 6.4$ s, and $\lambda = 0.30$, $H_s = 0.72$ m, and $T_p = 16$ s, as shown at left in Figure 15. There was also a significant current present, with mean components of 0.14 m/s in the dominant wave direction and 0.44 m/s in the transverse direction. For the present calculations, the mean current was included in the drag term of the Morison equation.

The measured and computed force spectra are shown at right in Figure 15. The variance is correctly predicted. The analysis also predicts correctly that the energy in the wave spectrum is shifted to higher frequencies; but underestimates the extent to which this is so.

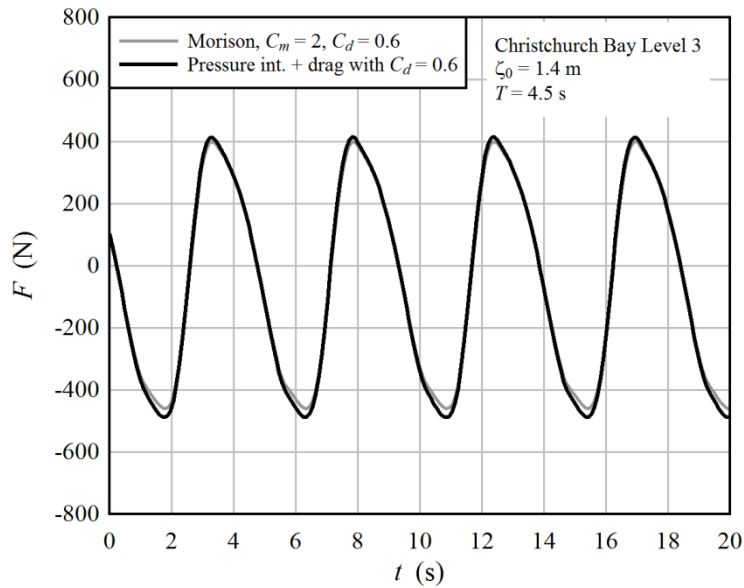


Figure 14: Comparison of the present method (pressure integration plus drag) with a standard Morison formulation, for a submerged section of a small cylinder, where the Morison equation is expected to be valid.

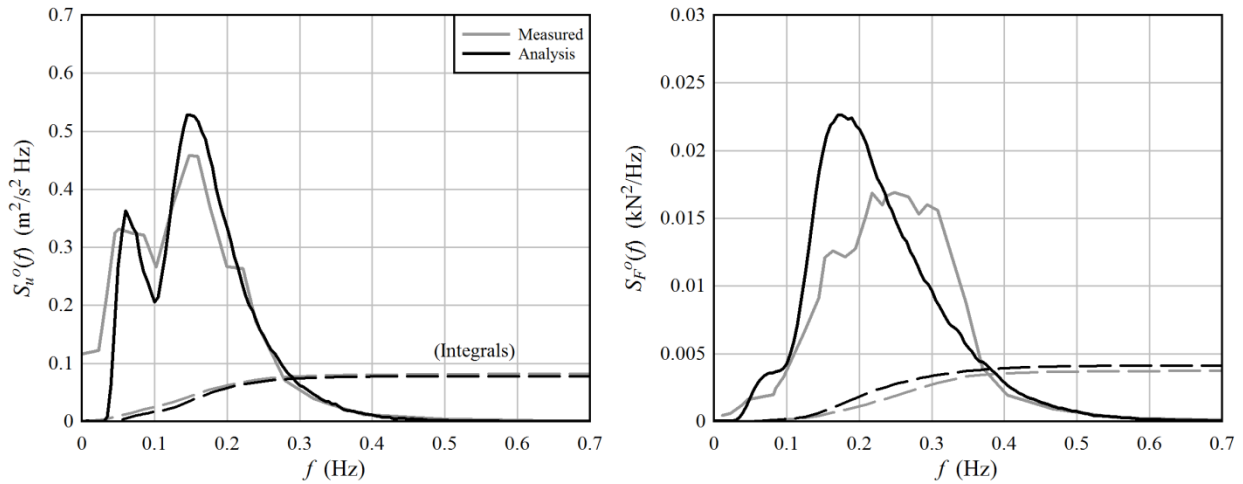


Figure 15: Measured and computed spectra for the Christchurch Bay cylinder, with all joints locked. Data from Najafian *et al.* [31]. At left: the calibrated water particle velocity spectra. At right: spectra of forces in the dominant wave direction.

Herfjord and Nielsen [19] provide an analytical estimate of first- and second-order contributions to the total wave loads on a 325 m draft, 15 m diameter spar. Figure 16 compares the wave load spectra for a case where $H_s = 9.8$ m and $T_p = 15.1$ s. The first-order wave loads are in agreement. The high-frequency tail of the present method lies somewhat under the sum-frequency load spectrum reported by Herfjord and Nielsen. A comparison between the present method and MacCamy and Fuchs' purely first-order solution (no drag, no stretching, linear pressure) indicates that the sum-frequency effects are so small that they are washed out by numerical noise in the first-order spectrum. In any case, at high frequencies, the spectra obtained by methods which consider diffraction lie far below the Morison force spectrum, relatively speaking. The reason for this is

primarily the phase offset, from one part of the cylinder to another, of the high-frequency wave components.

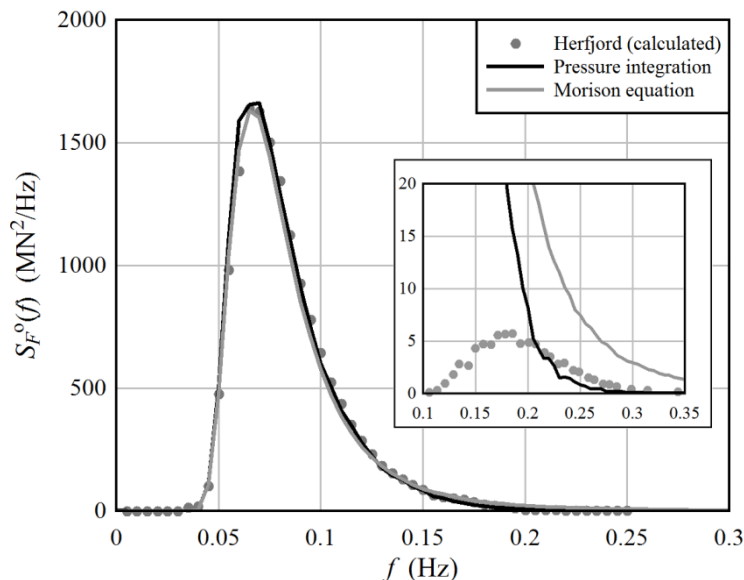


Figure 16: A comparison of theoretical wave load calculations on a 325 m draft, 15 m diameter spar. Pierson-Moskowitz spectrum, $H_s = 9.8$ m, $T_p = 15.1$ s. The inset is a magnification of the plot. The results from Herfjord and Nielsen [19] in the main plot are the first-order forces, and in the inset are the sum-frequency forces.

Herfjord and Nielsen also report the results of a series of wave tank experiments aimed at measuring the first- and second-order forces of solitary sinusoidal waves and pairs of waves. The experiment consisted of a 0.2 m diameter cylinder in a 0.9 m deep wave tank. The cylinder was pinned at the floor, and attached to a force transducer above the free surface. It was not specified at what distance above the free surface the force transducer was attached to the cylinder; this is a critical parameter, as it influences what fraction of the total force passes through the force transducer, as opposed to the pin joint at the base. Good agreement with the first-order wave forces was found using a height of 0.22 m above the free surface.

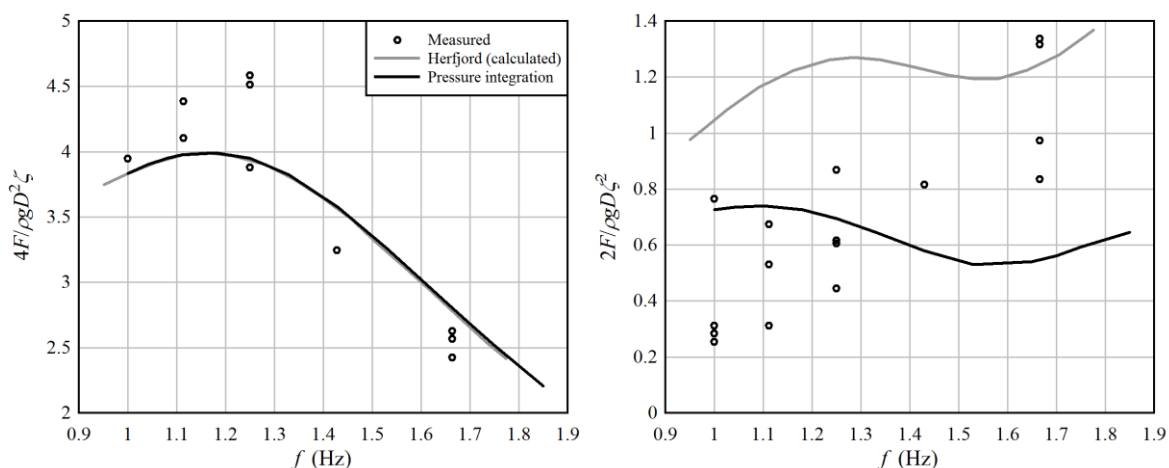


Figure 17: Wave forces on a cylinder, for monochromatic (single-frequency) sinusoidal waves, from Herfjord and Nielsen [19]. Experiment, amplitudes between 1 and 2 cm. Analysis, amplitude of 1.5 cm. At left: first-order forces. At right: sum-frequency forces.

The results for first-order and sum-frequency forces are shown in Figure 17. The forces were determined by taking the Fourier transform of the force time history, and extracting the amplitudes of the first and second frequency components. The sum-frequency forces computed by the present method lie nearer the data for longer waves, whereas the method of Herfjord and Nielsen provides better estimates for short, steep waves. It is noted that for the given experimental setup, a 1 Hz (1 s) wave is near the expected range of validity of linear wave kinematics, whereas a 1.67 Hz (0.6 s) wave is outside the range of steepness for which linear theory is recommended [11].

Herfjord and Nielsen also report results for a case with a bichromatic (dual-frequency) wave: an amplitude of 2 cm at 1.11 Hz, and an amplitude of 1.3 cm at 1.67 Hz. Figure 18 shows the results. As was the case in the monochromatic waves of Figure 17, the present method gives sum-frequency forces which are roughly half those of Herfjord and Nielsen, and the comparison with data indicates that the relative accuracy depends on the frequency. In the case of bichromatic waves, the trend in relative accuracy with frequency lacks a readily-identifiable pattern.

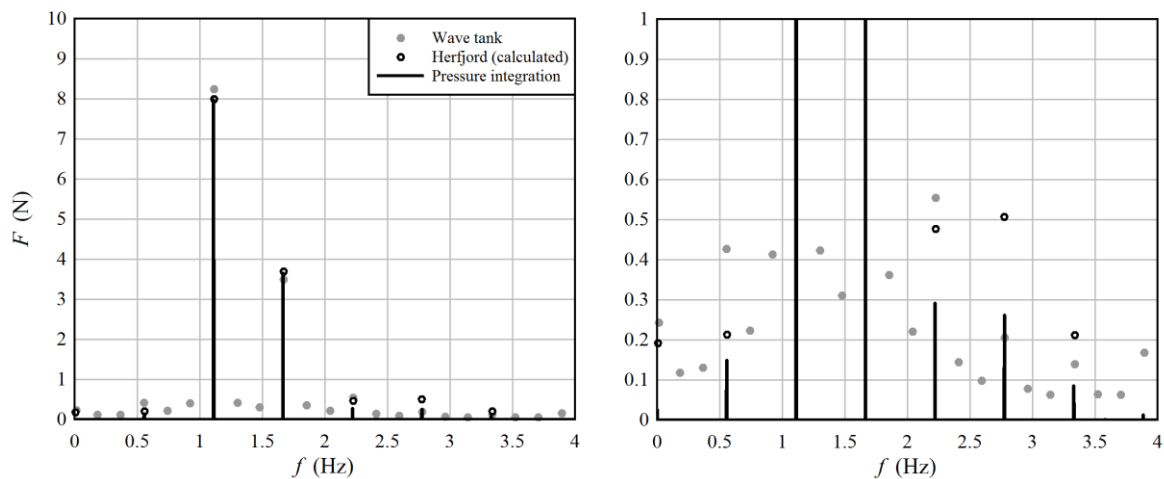


Figure 18: Data from Herfjord and Nielsen [19] Figures 10 and 11, with the addition of results using the present method. Bichromatic wave, with an amplitude of 2 cm at 1.11 Hz, and an amplitude of 1.3 cm at 1.67 Hz.

Isaacson and Baldwin [20] report wave load spectra measured on a 10 cm section of a 0.17 m diameter cylinder, located in the splash zone just above the mean free surface. The water depth was 2 m. Figure 19 shows results for a fairly severe wave climate, with H_s of 0.43 m and T_p of 3.13 s. Both the Morison equation and the present method are in the vicinity of the measured data, with the former closer at high frequencies and the latter generally closer at wave- and sum-frequencies.

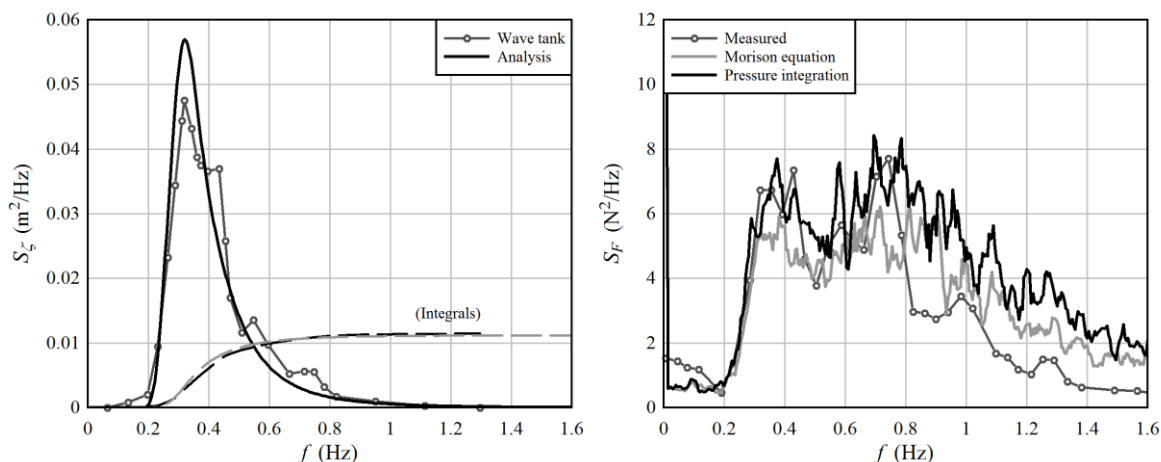


Figure 19: Wave load spectra in the splash zone, on a section of the cylinder which is alternately dry and submerged. Data from Isaacson and Baldwin [20]. At left: calibration of the wave spectrum for analysis. At right: load spectra at the 10 cm section of the cylinder.

In conclusion, by extending the Morison equation with a calculation of the full first-order potential, while retaining the concept of Wheeler stretching, the method described in Sections 3.2 through 3.4 reproduces the results of the Morison equation when the latter is expected to be valid; while the extended method is also valid for large-diameter monopiles. Otherwise, the strengths and weaknesses of the two methods are similar. In particular, a strength of the present method is that it is straightforward to include the influence of viscous drag due to current, and, although there is uncertainty associated with combined wave and current loads, the uncertainties are most often investigated in the context of the Morison equation. A weakness of the present method is the use of linear wave kinematics, which limits the applicability to fatigue analysis, where the steepness of the waves is assumed to be small. More accurate time-domain methods are available in specialized hydrodynamics codes, and could be used in place of the present method to generate load spectra from time series, in the manner of Section 3.4.

3.6 Illustrative Results

For illustration, we consider a 9 m diameter monopile foundation in 30 m water depth, representative of a large (say, 10 MW) offshore wind turbine. Nodal load spectra were generated for each nonzero combination of H_s and T_p shown in Table I.

Figure 20 shows the auto-spectra of nodal loads for two wave states. At left is a typical wave state, and at right an extreme wave state. Interestingly, the energy in a frequency band of 0.20 to 0.25 Hz, characteristic of the first fore-aft and side-to-side resonance frequencies of the tower, is comparable between the two wave states. In the typical wave state, the first-order loads dominate this frequency band, whereas in the extreme wave state, it is the sum-frequency loads which dominate.

The cross-spectra are not plotted, as these appear similar to the auto-spectra, and are nearly in-phase over the wave- and sum-frequency bands.

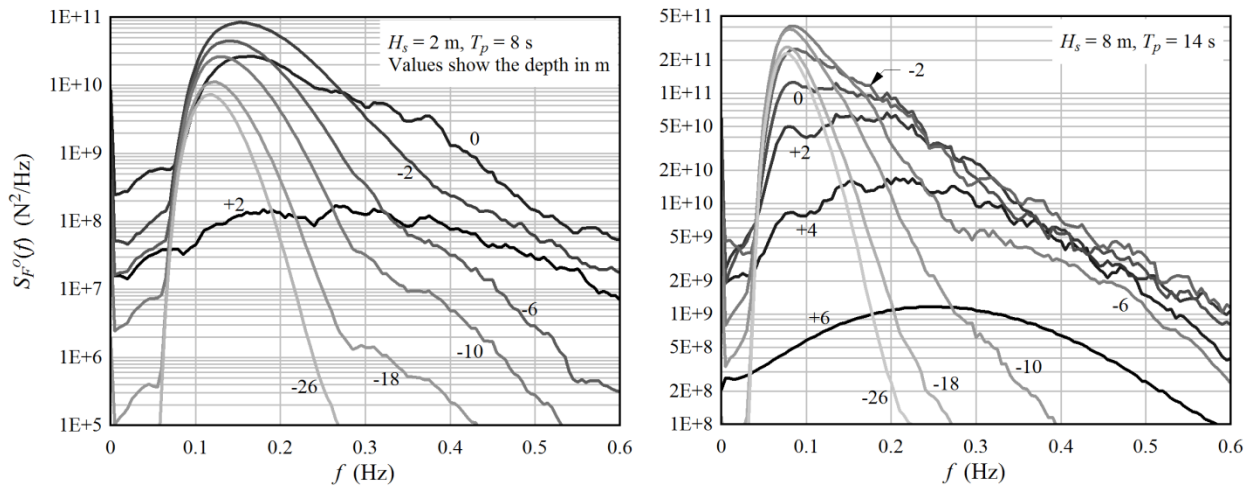


Figure 20: Auto-spectra of nodal wave loads under a common wave state (at left) and an extreme wave state (at right). Note that the energy in the spectra at a tower resonance frequency band of 0.20 to 0.25 Hz is of a comparable magnitude. The results are normalized to an element length (distance between adjacent nodes) of 2 m; not all nodes are shown in the plots.

Spectra of the total wave forces on the foundation were computed by summing the time series of forces from the individual nodes. Figure 21 compares the load spectra obtained by the present method (pressure integration) with those from the Morison equation. The Morison equation predicts a significantly greater loading in the tower resonance frequency band of 0.20 to 0.25 Hz. The principal reason is that the Morison equation does not account for the phase offset of the waves over the extent of the cylinder, as shown in Figure 22.

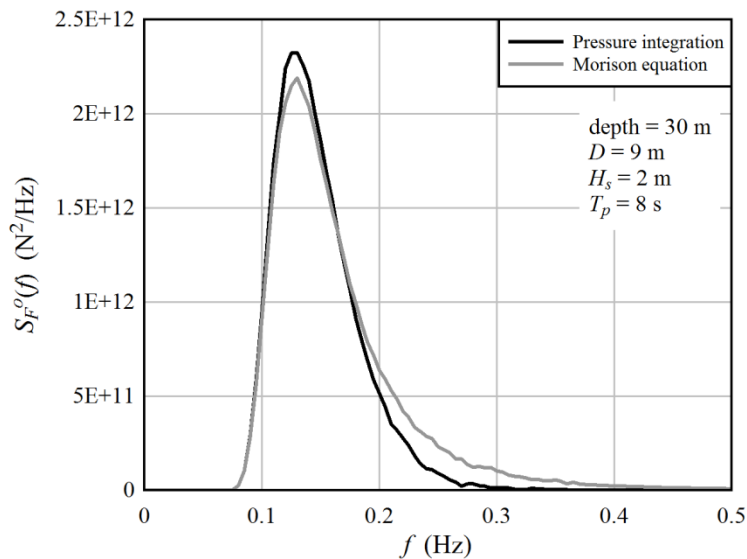


Figure 21: The spectrum of the total (summed) wave forces on the monopile, comparing the present method with the Morison equation.

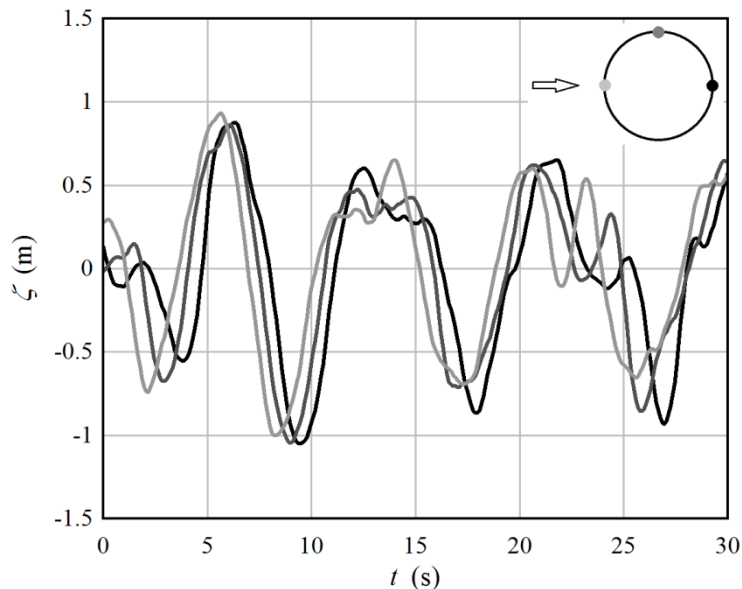


Figure 22: A sample of wave elevations computed at three points about the pile. $H_s = 2$ m, $T_p = 8$ s.

4 Conclusions

Methods have been developed for the calculation of environmental loads, as input to the STAS wind power plant analysis program. A spectral model of rotationally-sampled turbulence was extended using the multi-blade coordinate transformation, in order to give the correct frequency spectra, dominated by multiples of 3P, seen by the support structures. The result is a matrix of blade nodal turbulence spectra, in multi-blade coordinates, incorporating the appropriate cross-spectra between all degrees-of-freedom.

A method was also developed for generating the cross-spectra of wave loads between the nodes of the foundation. The often-used Morison equation was extended using a full first-order potential solution. The potential solution is valid both for small-diameter cylinders – for which the results of the Morison equation are reproduced – and for large-diameter cylinders whose diameter is on the same order as the wavelength. The computation of loads is performed in the time-domain, and subsequently transformed to the frequency domain. The first-order velocity profiles are stretched to the instantaneous free-surface, and velocity-squared terms are retained in Bernoulli's equation, in order to capture the most important sum-frequency effects which may excite tower resonance. The method was validated by comparison against published calculations, laboratory experiments, and field measurements. Due to the use of first-order wave kinematics, the method is intended to be used for stochastic fatigue analysis, and may underpredict extreme loads.

References

- [1] Abramowitz M, Stegun IA (editors). *Handbook of Mathematical Functions*. Dover, 1965.
- [2] Bir G. Multiblade coordinate transformation and its application to wind turbine analysis. Paper NREL/CP-500-42553, National Renewable Energy Laboratory, 2008. Presented at the ASME Wind Energy Symposium, Reno, NV, USA, January 7-10, 2008.

- [3] Burrows R, *et al.* Morison wave force coefficients for application to random seas. *Applied Ocean Research* 19 (1997) 183-199.
- [4] Burton T, *et al.* *Wind Energy Handbook*. Wiley, 2001.
- [5] Calaf M, *et al.* Large eddy simulation study of fully developed wind-turbine array boundary layers. *Physics of Fluids* 22 (2010) 015110.
- [6] Chakrabarti SK. Non-linear wave effects on large offshore structures. *Proceedings of the Second International Symposium on Ocean Engineering and Ship Handling*, Swedish Maritime Research Center, 1983, pp 19-49.
- [7] Chakrabarti SK (editor). *Handbook of Offshore Engineering*. Elsevier, 2005.
- [8] Coleman RP, Feingold AM. Theory of self-excited mechanical oscillations of helicopter rotors with hinged blades. Report NACA-TR-1351, National Advisory Committee for Aeronautics, 1958.
- [9] Connell JR. The spectrum of wind speed fluctuations encountered by a rotating blade of a wind energy conversion system. *Solar Energy* 29 (1982) 363-375.
- [10] Davidson PA. *Turbulence: An Introduction for Scientists and Engineers*. Oxford University Press, 2004.
- [11] DNV, *Environmental Conditions and Environmental Loads*. Recommended Practice DNV-RP-C205, Det Norske Veritas, April 2007.
- [12] Eatock Taylor R, Hung SM. Wave drift enhancement effects in multi column structures. *Applied Ocean Research* 7 (1985) 128-137.
- [13] Eatock Taylor R, Rajagopalan A. Dynamics of offshore structures, Part I: Perturbation analysis. *Journal of Sound and Vibration* 83 (1982) 401-416.
- [14] Eatock Taylor R, Rajagopalan A. Load spectra for slender offshore structures in waves and current. *Earthquake Engineering and Structural Dynamics* 11 (1983) 831-842.
- [15] Fischer T, *et al.* *Upwind Design Basis*. UpWind Consortium, 2010.
- [16] Gudmestad OT, Connor JJ. Linearization methods and the influence of current on the nonlinear hydrodynamic drag force. *Applied Ocean Research* 5 (1983) 184-194.
- [17] Hansen MH. Improved modal dynamics of wind turbines to avoid stall-induced vibrations. *Wind Energy* 6 (2003) 179-195.
- [18] Hansen MH. Aeroelastic stability analysis of wind turbines using an eigenvalue approach. *Wind Energy* 7 (2004) 133-143.
- [19] Herfjord K, Nielsen FG. Non-linear wave forces on a fixed vertical cylinder due to the sum frequency of waves in irregular seas. *Applied Ocean Research* 8 (1986) 8-21.
- [20] Isaacson M, Baldwin J. Measured and predicted random wave forces near the free surface. *Applied Ocean Research* 12 (1990) 188-199.
- [21] Kim CH. *Nonlinear Waves and Offshore Structures*. World Scientific, 2008.
- [22] Kristensen L, Frandsen S. Model for power spectra of the blade of a wind turbine measured from the moving frame of reference. *Journal of Wind Engineering and Industrial Aerodynamics* 10 (1982) 249-262.
- [23] Kristensen L. Power spectra and cross-spectra as seen from the moving blade of a wind turbine. *Journal of Wind Engineering and Industrial Aerodynamics* 12 (1983) 245-250.
- [24] MacCamy RC, Fuchs RA. Wave Forces on Piles: A Diffraction Theory. Technical Memorandum No. 69, Beach Erosion Board, Corps of Engineers (USA), 1954.
- [25] Malhotra AK, Penzien J. *Stochastic Analysis of Offshore Tower Structures*. Report EERC 69-6, University of California, Berkeley, 1969.
- [26] Meneveau C. The top-down model of wind farm boundary layers and its applications. *Journal of Turbulence* 13 (2012) 1-12.

- [27] Merz KO. *Conceptual Design of a Stall-Regulated Rotor for a Deepwater Offshore Wind Turbine*. Doctoral Theses at NTNU 2011:191, Norwegian University of Science and Technology, Trondheim, Norway, 2011.
- [28] Merz KO, *et al.* A simple frequency-domain method for stress analysis of stall-regulated wind turbines. *Wind Energy* 15 (2012) 773-798.
- [29] Merz KO. *A Linear State-Space Model of an Offshore Wind Turbine, Implemented in the STAS Wind Power Plant Analysis Program*. Report TR A7474, SINTEF Energy Research, 2015.
- [30] Miles J, Gilbert F. Scattering of gravity waves by a circular dock. *Journal of Fluid Mechanics* 34 (1968) 783-793.
- [31] Najafian G, *et al.* The UK Christchurch Bay compliant cylinder project: analysis and interpretation of Morison wave force and response data. *Applied Ocean Research* 22 (2000) 129-153.
- [32] Newman JN. *Marine Hydrodynamics*. MIT Press, 1977.
- [33] Press WH, *et al.* *Numerical Recipes – The Art of Scientific Computing*. Third Edition, Cambridge University Press, 2007.
- [34] Stol KA, *et al.* A comparison of multi-blade coordinates transformation and direct periodic techniques for wind turbine control design. AIAA 2009-479, 47th AIAA Aerospace Sciences Meeting, Orlando, FL, USA, January 5-8, 2009.
- [35] Sørensen P. *Frequency Domain Modelling of Wind Turbine Structures*. Report Risø-R-749(EN), Risø National Laboratory (DTU), Denmark, 1994.
- [36] Sørensen P, *et al.* Wind models for simulation of power fluctuations from wind farms. *Journal of Wind Engineering and Industrial Aerodynamics* 90 (2002) 1381-1402.
- [37] Tickell RG, Bishop JR. Analysis of waves and wave forces at the Christchurch Bay Tower. *Proceedings of the 4th International Offshore Mechanics and Arctic Engineering Symposium*, Dallas, TX, USA, February 1985, pp 142-150.
- [38] van Engelen T, *et al.* TURBU Offshore, Computerprogramma voor frequentiedomein analyse van horizontale as offshore windturbines, Fase I: Modelbeschrijving. (In Dutch.) Report ECN-C--02-073, Energy Research Centre of the Netherlands, 2002.
- [39] van Engelen T, Braam H. TURBU Offshore, Computer Program for Frequency Domain Analysis of Horizontal Axis Offshore Wind Turbines. Report ECN-C--04-079, Energy Research Centre of the Netherlands, 2004.
- [40] Varma A, Morbidelli M. *Mathematical Methods in Chemical Engineering*. Oxford University Press, 1997.
- [41] Wheeler JD. Method for calculating forces produced by irregular waves. *Journal of Petroleum Technology* 22 (1970) 359-367.



Technology for a better society
www.sintef.no